Stress induces cytoprotective TDP-43 nuclear bodies through lncRNA *NEAT1*-promoted phase separation

Authors: Chen Wang[1,2,*], Yongjia Duan[1,2,*], Gang Duan[1,2,*], Zhiwei Ma[1,†], Kai Zhang[1,2], Xue Deng[1,2], Beituo Qian[1,2], Jinge Gu[1,2], Qiangqiang Wang[1], Shuang Zhang[1], Lin Guo[3], Cong Liu[1,2,§], and Yanshan Fang[1,2,6,§]

Affiliations:

[1]Interdisciplinary Research Center on Biology and Chemistry, Shanghai Institute of Organic Chemistry, Chinese Academy of Sciences, Shanghai 201210, China

[2]University of Chinese Academy of Sciences, Beijing, 100049, China,

[3]Department of Biochemistry and Molecular Biology, Thomas Jefferson University, Philadelphia, PA 19107, USA

*These authors contributed equally

[†]Current address: West China School of Basic Medical Sciences and Forensic Medicine, Sichuan University, Chengdu, 610041, China

[§]Correspondence to:

Cong Liu: liulab@sioc.ac.cn

Yanshan Fang: fangys@sioc.ac.cn

Tel: +86-21-6858.2510

Fax: +86-21-6858.2502

Short title (<50 characters): Phase-separated TDP-43 NBs mitigate stress

Keywords: TDP-43, nuclear body, RNP granule, phase separation, lncRNA *NEAT1*

***Word count**: ~6500 words (excluding the title page, abstract, references and figure legends)*

Graphic Abstract

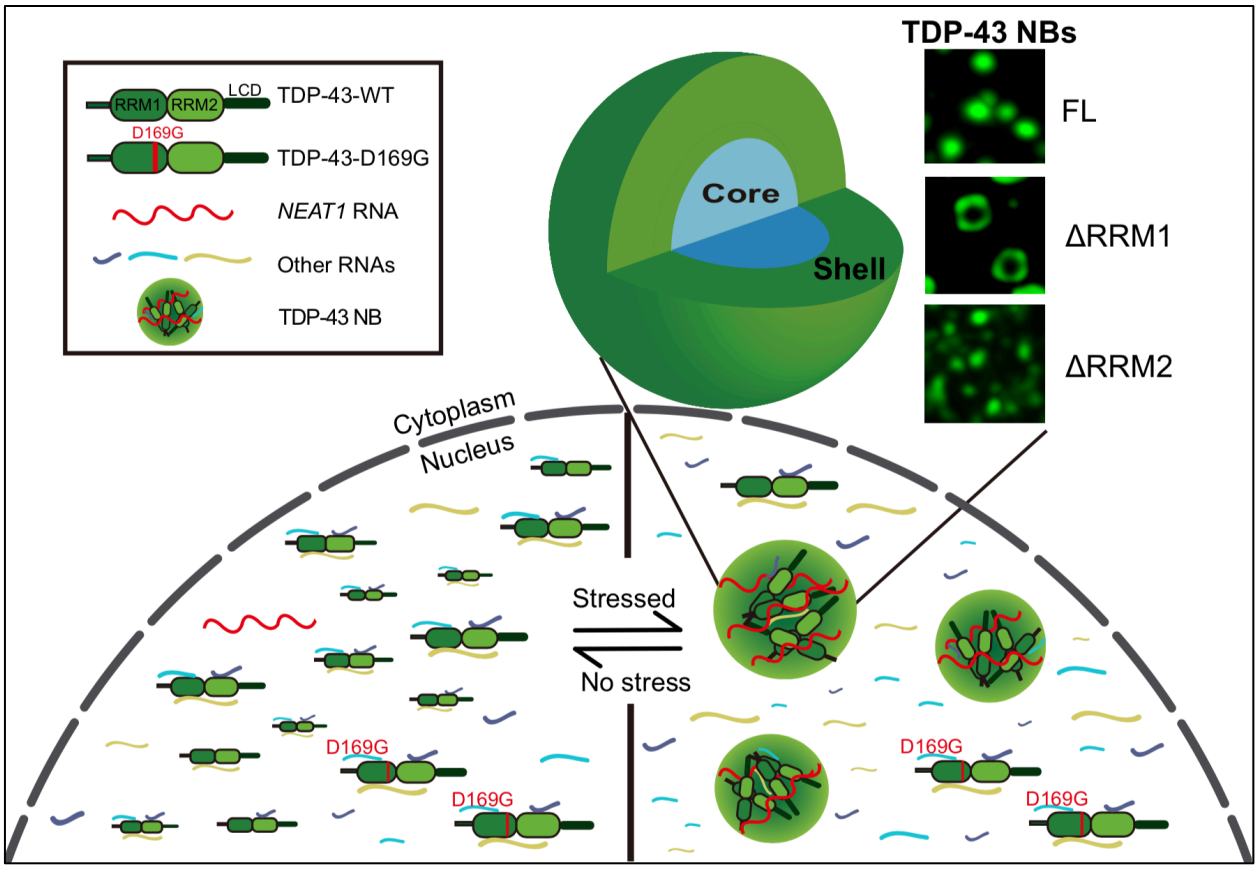

Highlights *(Up to four bullet points. The length of each highlight cannot exceed 85 characters, including spaces)*

- TDP-43 forms reversible, LD-like NBs alleviating cytotoxicity and neurodegeneration
- The two RRMs act antagonistically to maintain a core-shell architecture of TDP-43 NBs
- LncRNA *NEAT1* is upregulated in stressed neurons, which promotes TDP-43 LLPS
- ALS-causing mutation D169G abolishes *NEAT1*-induced TDP-43 LLPS and NBs

SUMMARY (< 150 words)

Despite the prominent role of TDP-43 in neurodegeneration, its physiological and pathological functions are not fully understood. Here, we report an unexpected function of TDP-43, which forms dynamic, reversible, droplet-like nuclear bodies (NBs) in response to stress, and the formation of NBs alleviates TDP-43-mediatd cytotoxicity and neurodegeneration in cell and *Drosophila* models of amyotrophic lateral sclerosis (ALS). Super-resolution microscopy reveals a "core-shell" architecture of TDP-43 NBs, which is maintained by the two RRMs antagonistically. Further, TDP-43 NBs are partially colocalized with nuclear paraspeckles and the paraspeckle scaffolding lncRNA *NEAT1* is dramatically upregulated in stressed neurons. Moreover, increase of *NEAT1* promotes TDP-43 liquid-liquid phase separation (LLPS) *in vitro*. Finally, we uncover that the ALS-associated mutation TDP-43^{D169G} impairs *NEAT1*-induced phase separation, causing a specific defect in the assembly of TDP-43 NBs but not stress granules. Together, our findings propose a stress-mitigating role and mechanism for TDP-43 NBs, whose dysfunction may contribute to ALS pathogenesis.

INTRODUCTION

Amyotrophic lateral sclerosis (ALS) is a progressive motor neuron disease characterized by the degeneration of motor neurons in the brain and spinal cord, which leads to fatal paralysis generally within 2–5 years after diagnosis (*1*,*2*). Missense mutations in the gene *TARDBP* encoding the trans-activation response element (TAR) DNA-binding protein 43 (TDP-43) predispose to familial ALS, and protein inclusions containing TDP-43 in the affected motor neurons are a pathological hallmark of ALS (*3*, *4*). TDP-43 is a nuclear protein but can shuttle between the nucleus and the cytoplasm. It has a nuclear localization signal (NLS), a nuclear export signal (NES), two canonical RNA recognition motifs (RRMs) that bind to nucleic acids, and a C-terminal low complexity domain (LCD) that mediates protein-protein interactions and is enriched of disease-associated mutations (*4*, *5*). TDP-43 is engaged in a variety of ribonucleoprotein (RNP) complexes and plays an important role in RNA processing and homeostasis (*6-10*). In addition, TDP-43 is known to participate in cytoplasmic stress granules (SGs), which may undergo aberrant phase transition and promote the formation of solid protein aggregates in diseased conditions (*11-14*).

Nuclear bodies (NBs) are dynamic, membraneless nuclear structures that concentrate specific nuclear proteins and RNAs and play an important role in maintaining nuclear homeostasis and RNA processing (*15*, *16*). Increasing evidence suggests the association of TDP-43 with a variety of NBs, such as paraspeckles (*17-19*), gemini of coiled bodies (GEMs) (*20*), nuclear stress bodies (*21*), interleukin-6 and -10 splicing activating compartment bodies (InSAC bodies) (*22*), and omega speckles (*23*). Notably, in the nucleus of spinal motor neurons of sporadic ALS patients, TDP-43 is found colocalized with paraspeckles and the occurrence of paraspeckles is specifically increased in the early phase of the disease (*18*). In addition, excessive formation of dysfunctional paraspeckles is also observed in the spinal neurons and glia of ALS-FUS patients (*24*). Although it is clear that TDP-43 is present in NBs that sometimes accompanies neurodegeneration, our understanding of the function of TDP-43 in NBs and the contribution of NBs to ALS pathogenesis is still rudimentary.

Recent studies indicate that liquid-liquid phase separation (LLPS) of RNA-binding protein (RBPs) drives the assembly of liquid droplet (LD)-like, membraneless RNP granules in the cytoplasm and nucleoplasm (*25-29*). Several ALS-related RBPs including TDP-43, FUS, hnRNP A1, hnRNP A2 and TIA1 are shown to phase separate *in vitro* (*14*, *30-35*). The intrinsically disordered LCD domains of the RBPs are thought to mediate the LLPS (*28*, *31*, *36-38*) and posttranslational protein modifications play an important role in determining the biophysical and biological properties of the phase behavior of the RBPs (*34*, *39-46*). In addition to the LCD, recent studies reveal that RNA is of vital importance in regulating the LLPS (*47*, *48*), which can either suppress or promote phase separation depending on the contents and concentrations of the RNAs (*25*, *49-51*).

In this study, we find that various cellular stresses induce TDP-43 to form distinct, highly dynamic and reversible NBs, which not only attenuate the cytotoxicity of TDP-43 in mammalian cells but also ameliorate neurodegeneration and behavioral deficits in a *Drosophila* model of ALS. Further investigation with super-resolution microscopy reveals the unexpected opposing functions of the two RRMs in maintaining the core-shell architecture of TDP-43 NBs. Furthermore, we demonstrate a crucial role of the paraspeckle scaffolding RNA nuclear-enriched abundant transcript 1 (*NEAT1*) in promoting TDP-43 LLPS *in vitro*, which is compromised by the ALS-causing mutation D169G, leading to a defect in forming TDP-43 NBs. Together, our findings demonstrate how stress induces the assembly of TDP-43 NBs in the generally “suppressive” nucleoplasm environment and suggest the involvement of dysfunctional TDP-43 NBs in ALS pathogenesis.

RESULTS

Arsenic stress induces dynamic and reversible TDP-43 NBs

TDP-43 protein is predominantly localized to the nucleus but can shuttle between the nucleus and the cytoplasm. In response to cellular stress, TDP-43 is recruited to cytoplasmic SGs (*11*). Interestingly, in an earlier related work of our group (*46*), we noticed that although arsenite, a commonly used experimental reagent to raise cellular stress (*52*), induced TDP-43^{+} cytoplasmic SGs, the majority of TDP-43 signal remained in the nucleus. Furthermore, in a great portion of the cells, the nuclear TDP-43 lost the normal diffused pattern and instead exhibited a distinct granular appearance (Movie S1 and Fig. 1, A and B).

A membraneless nuclear structure fulfills the requirements of NBs if it is: (1) microscopically visible, (2) enriched with specific nuclear factors, and (3) continuously exchanging the contents with the surrounding nucleoplasm (*15*). Indeed, arsenite-induced TDP-43 nuclear granules were microscopically visible (Fig. 1). Further examination by immunocytochemistry indicated that these arsenite-induced nuclear granules were colocalized or partially colocalized with several known types of NBs, especially paraspeckles marked by splicing factor proline-glutamine rich (SFPQ) (Fig. S1). These results suggest that cellular stress may be involved in the translocation of TDP-43 into NBs such as paraspeckles, similar to that found in the spinal motor neurons of ALS patients (*18*).

To examine if stress-induced TDP-43 nuclear granules were liquid-like and could exchange with surrounding nucleoplasm, we performed the fluorescence recovery after photobleaching (FRAP) analysis in *live* cells using a green fluorescent protein (GFP)-tagged TDP-43 (GFP-TDP-43). To induce TDP-43 nuclear granules, cells were pre-treated with arsenite (250 μM) for 30 minutes before photobleaching. The fluorescence of GFP-TDP-43 nuclear granules was rapidly recovered after photobleaching, reaching ~50% of the pre-bleaching intensity in ~65 seconds (Movie S2 and Fig. 1, C and D). Thus, these data indicate that stress-induced TDP-43 nuclear granules are liquid-like and highly dynamic. Together, they fulfilled all the above three requirements and are thereafter called TDP-43 NBs in this study.

Next, we determined whether stress-induced TDP-43 NBs were reversible using arsenite washout assay. After arsenite removal, the stress-induced TDP-43 NBs gradually disappeared and eventually recovered to nearly diffused pattern like that before the arsenite treatment (Fig. 1E). Our quantitative analyses indicated that both the percentages of cells with TDP-43 NBs and the number of TDP-43 NBs per cell decreased in a time-dependent manner after arsenite washout (Fig. 1, F to H). Of note, there were considerably more cells with TDP-43 NBs than TDP-43-associated (TDP-43$^+$) SGs (Fig. 1B) and overwhelmingly more TDP-43 NBs than TDP-43$^+$ SGs per cell before the washout started (Fig. 1E, 0 min). Hence, although the percentages of cells with visible TDP-43 NBs were not markedly reduced when TDP-43$^+$ SGs became largely undetectable at 30 min after arsenite removal (Fig. 1, F and G), the average number of TDP-43 NBs per cell did significantly decrease (Fig. 1H). Together, our data indicate that arsenic stress-induced TDP-43 NBs are reversible as that of SGs upon the relief of stress.

Formation of TDP-43 NBs as a general cellular stress mechanism

Next, we examined if endogenous TDP-43 could also form NBs upon arsenic stress. We found that in most cells, endogenous TDP-43 was present as evenly distributed while some cells showed spontaneous small granules (Fig. S2A). The arsenite treatment led to the formation of larger and more NBs in a significantly increased number of cells (Fig. S2, A and B). In addition, we observed stress-induced TDP-43 NBs also in *in vitro* cultured mouse primary neurons (Fig. S2, C and D). Thus, the formation of TDP-43 NBs is not an artificial effect due to TDP-43 overexpression or the use of non-neuronal cell lines. Moreover, it was previously reported that heat shock-induced reversible nuclear TDP-43 “aggregations” were colocalized with the marker of nuclear stress bodies (*21*). These observations raised the possibility that the formation of TDP-43 NBs might be a general stress response mechanism in the nucleus. Indeed, we found that disturbance of the nuclear homeostasis by inhibiting nuclear export with leptomycin B (LMB) also effectively induced endogenous TDP-43 to form NBs (Fig. 2, A and B).

To further determine whether blocking nuclear export of TDP-43 itself was sufficient to induce the formation of TDP-43 NBs, we generated mutations in the NLS and the NES of TDP-43, respectively (NLS^{mut} and NES^{mut}; Fig. 2C). Under normal conditions, wild-type (WT) TDP-43 was mostly present in diffused pattern in the nucleus with rare occurrence of spontaneous TDP-43 NBs (Fig. 2, D to F). As expected, the NLS^{mut} TDP-43 was predominantly cytoplasmic and thus the chance of TDP-43 NBs with the NLS^{mut} was even lower than that of the WT (Fig. 2, D to F). In contrast, the NES^{mut} was exclusively nuclear and formed TDP-43 NBs even in the absence of arsenite, heat shock or LMB treatment (Fig. 2, D to F). Furthermore, the solubility of TDP-43-NES^{mut} protein was significantly reduced, as more than half of the protein was insoluble in radioimmunoprecipitation assay buffer (RIPA) (Fig. 2, G and H).

The marked reduction in the solubility of the NES^{mu} protein raised the question whether the TDP-43-NES^{mut} NBs were still in a dynamic, liquid-like state or became solid “aggregates”. To address this question, we examined the stability of WT and mutant TDP-43 proteins by treating cells with protein synthesis inhibitor cycloheximide (CHX) (*53*). We found that the RIPA-soluble TDP-43 protein was rather stable, as none of the WT, NLS^{mut} or NES^{mut} TDP-43 in the soluble fractions showed significant turnover in 24 h after CHX treatment (Fig. S3, A to D). In contrast, the RIPA-insoluble fraction of TDP-43-NES^{mut} decreased rapidly upon CHX inhibition and became almost undetectable within 24 h (Fig. S3, A to D). Meanwhile, we found that the treatment with CHX led to rapid disassembly of TDP-43-NES^{mut} NBs and reduction in the number of TDP-43-NES^{mut} NBs per cell (Fig. S3, E and F). These results suggest that the RIPA-insoluble TDP-43-NES^{mut} NBs are in a reversible, liquid-like state rather than solid “aggregates”. A similar observation of misfolded proteins entering the liquid-like, granular nucleolus under stress was recently reported, which may function as a phase-separated protein quality control compartment (*54*).

Next, we further examined how disturbance of the cellular proteostasis by blocking protein turnover impacted on this process. We inhibited proteasome-mediated protein degradation by MG132, which led to a significant increase in the RIPA-insoluble fraction of the NES^{mut} as well as

that of the WT TDP-43 protein (Fig. S4, A to D). In contrast, blocking autophagic flux by chloroquine (CQ) did not significantly affect the levels of insoluble TDP-43 (Fig. S4, E to H). Thus, the turnover of TDP-43 NBs did not rely on the autophagy-lysosomal pathway, which was more commonly used to clear misfolded protein aggregates (*55*, *56*). Together, our data indicate that TDP-43 NBs are dynamic, reversible and sensitive to the environment of surrounding nucleoplasm, which may act as a general cellular mechanism to various stresses.

Formation of TDP-43 NBs alleviates the cytotoxicity

We were keen to understand the functional significance of forming TDP-43 NBs. Was it a "protective" mechanism for cells, like that of SGs? Indeed, we found that overexpression (OE) of WT or NLS^{mut} TDP-43 but not the NB-forming NES^{mut} in human 293T cells led to decreased cell viability (Fig. 3A). To further confirm that the formation of TDP-43 NBs was required for the cytotoxicity-antagonizing effect rather than simply restricting TDP-43 in the nucleus, we sought for alternative approaches to promote or suppress TDP-43 NBs without disrupting its nucleocytoplasmic transport. It was previously shown that an acetylation-mimic K145/192Q mutation of TDP-43 impaired the RNA-binding and promoted the formation of TDP-43 protein inclusions in both the nucleus and the cytoplasm, whereas the acetylation-deficient K145/192R mutation suppressed that (*40*). Hence, we generated the K145/192Q mutation in WT TDP-43 (Fig. 3B) and the K145/192R mutation in TDP-43-NES^{mut} (Fig. 3C).

Indeed, the K145/192Q mutation led to the formation of TDP-43 NBs without affecting the nucleocytoplasmic distribution of TDP-43 and that was in the absence of LMB or arsenite treatment (Fig. 3, D, D', F, and H). And importantly, the NB-promoting K145/192Q mutation alleviated the cytotoxicity of WT TDP-43 (Fig. 3J), similar to the effect of the NES^{mut} (Fig. 3A). On the other hand, abolishing NB formation of the NES^{mut} by the K145/192R mutation (Fig. 3, E, E', G, and I) made the originally non-toxic TDP-43-NES^{mut} to exhibit marked cytotoxicity (Fig. 3K), like that of the WT TDP-43 (Fig. 3A). These data demonstrate that the formation of TDP-43 NBs

reduces the cytotoxicity and increases the cell viability, therefore potentially acting as a "protective" mechanism to help cells survive stressed or diseased conditions.

TDP-43-NES^{mut} forms neuronal NBs *in vivo* and mitigates neurodegeneration in a *Drosophila* model of ALS

To validate our findings in an *in vivo* model, we utilized the binary GAL4-UAS system (*57*) to generate transgenic flies in order to express WT, NLS^{mut} or NES^{mut} human TDP-43 (hTDP-43) in a tissue-specific manner. The transgenes of WT and mutant UAS-*hTDP-43* were inserted in the same locus of the fly genome by ΦC31 integrase-mediated, site-specific integration (*58-60*). This approach avoided the location effect on transgene expression across different fly lines and allowed direct comparison between the WT and mutant TDP-43 flies. Immunohistochemistry analysis of the whole mount fly brains confirmed the predominant nuclear localization of the WT and NES^{mut} hTDP-43 in the fly neurons (*elav*-Gal4), whereas the NLS^{mut} was largely cytoplasmic (Fig. 4A). Consistent with the data in 293T cells (Fig. 2, D to F), the NES^{mut} hTDP-43 formed striking NBs in the nucleus of fly neurons (Fig. 4, A and B). Furthermore, the solubility of the hTDP-43-NES^{mut} protein extracted from the fly brains was significantly decreased (Fig. 4, C and D), which was also consistent with the results in the mammalian cells (Fig. 2, G and H).

We then examined the consequence of expressing WT, NLS^{mut} or NES^{mut} hTDP-43 in the fly eye (GMR-Gal4). WT and NLS^{mut} hTDP-43 flies showed slight eye degeneration at Day 5, as evidenced by the rough surface of the compound eyes and loss of pigment cells. At the same time point, however, the eyes of the NES^{mut} flies were largely unaffected and the degeneration score was much lower (0.4 ± 0.34) than that of WT hTDP-43 flies (1.5 ± 0.41, $P < 0.001$) (Fig. 4E). By Day 25, the eyes of WT and NLS^{mut} hTDP-43 flies further degenerated as a lot more pigment cells were lost and some eyes showed swelling especially in the NLS^{mut} hTDP-43 flies. Compared to WT hTDP-43 flies (2.5 ± 0.13), the eye degeneration of the NLS^{mut} flies was significantly worse (3.8 ± 0.17, $P < 0.001$), whereas that of the NES^{mut} flies was substantially milder (0.8 ± 0.14, $P < 0.001$) (Fig. 4E). Similar conclusions were obtained from the climbing

assay, which also showed a striking difference in the severity of neurotoxicity among WT, NLS^{mut} and NES^{mut} hTDP-43 flies. Expression of WT hTDP-43 in the fly motor neurons (D42-Gal4) caused an age-dependent decline of the climbing capability, which deteriorated much faster in the NLS^{mut} flies (Fig. 4F). The behavioral phenotype of NES^{mut} flies was the mildest, whose climbing capability was not statistically different from that of the control flies (UAS-*Luciferase*) at all time points examined (Fig. 4F). Together, these data indicate that the formation of TDP-43 NBs by the NES^{mut} alleviates the TDP-43-mediated neurodegeneration in an *in vivo Drosophila* model of ALS.

The role of the major functional domains of TDP-43 in the assembly of NBs

To understand how TDP-43 NBs were assembled, we generated truncated TDP-43 proteins, namely ΔLCD, ΔRRM1 and ΔRRM2, to determine how each major domain of TDP-43 is involved in regulating this process (Fig. S5A). It was previously shown that the intrinsically disordered LCD domain mediated protein-protein interaction and was critical for the formation of cytoplasmic SGs and protein aggregations (*31*, *61*). We found that both the WT and ΔLCD TDP-43 were mostly soluble (Fig. S5, B and C), however, the ΔLCD was unable to form NBs in response to LMB (Fig. S5, F to G'), indicating that the formation of TDP-43 NBs in cells requires the LCD domain.

Next, we examined the impact of deleting RRM1 or RRM2 on the assembly of TDP-43 NBs. The ΔRRM1 TDP-43 was largely soluble (Fig. S5D), while the ΔRRM2 showed a greatly increased insolubility (Fig. S5E). Interestingly, the ΔRRM1 TDP-43 formed large, ring-like structures in the nucleus even in the absence of LMB treatment (Fig. S5H). And, treatment with LMB did not promote further formation of the ring-like structures or trigger the formation of WT-like TDP-43 NBs (Fig. S5H'). ΔRRM2 TDP-43 looked similar to WT in cells without stress (Fig. S5I), whereas treating with LMB gave rise to a grainy appearance (Fig. S5I').

Super-resolution microscopy reveals a "core-shell" architecture of TDP-43 NBs maintained by the opposing functions of the two RRMs

To further characterize the nuclear structures formed by WT, ΔRRM1 and ΔRRM2 TDP-43, we utilized the Leica LIGHTNING SP8 confocal microscope to capture multicolor images in super-resolution down to 120 nm. Interestingly, we found that WT TDP-43 formed solid, mid-size NBs; ΔRRM1 was much larger, ring-shaped; and ΔRRM2 displayed a mesh-like structure with many smaller NBs (Fig. 5, A and B). Three-dimensional (3D) rendering revealed that WT TDP-43 NBs were not perfect "spheres" as ones might infer from the 2D images; rather, they were in oval or cylinder shapes in the cell. Unlike WT TDP-43, ΔRRM1 was mostly large, hollow "pillars"; whereas ΔRRM2 NBs looked similar to those of WT in 3D rendering. Further quantification confirmed that the average diameter of ΔRRM1 "rings" was drastically larger whereas that of ΔRRM2 NBs was noticeably smaller than that of WT TDP-43 (Fig. 5C).

Given the distinct morphology of the nuclear structures formed by ΔRRM1 and ΔRRM2 TDP-43, it was tempting to propose a "core-shell" architecture of TDP-43 NBs and the two RRMs might function antagonistically to maintain such a structure – the RRM1 pushed TDP-43 toward the core of NBs whereas the RRM2 pulled TDP-43 toward the shell (Fig. 5D). If this hypothesis were correct, ΔRRM1 TDP-43 that lacked the "centripetal force" of the RRM1 would be mainly distributed to the shell of NBs, while ΔRRM2 TDP-43 that lacked the "centrifugal force" would be mainly located in the core. To test this hypothesis, we co-expressed HA-Tagged WT TDP-43 with Myc-tagged WT, ΔRRM1 or ΔRRM2 TDP-43 and induced NB formation in 293T cells by LMB (Fig. 5, E to H). Indeed, ΔRRM1 formed a ring-like shell wrapping the co-expressed WT TDP-43 NBs (Fig. 5, F and J) and the diameter of the NBs was dramatically larger (Fig. 5N). The increased diameter was not simply due to overexpression of two folds of TDP-43 protein, as co-expression of WT TDP-43-HA and WT myc-TDP-43 did not show such effect (Fig. 5, E, I, and M). Consistent with our hypothesis, we found that ΔRRM2 co-expressed with the WT TDP-43 was mainly located in the core of NBs (Fig. 5, G and K) and the diameter was significantly smaller (Fig. 5O). The core-shell architecture could also be clearly seen when ΔRRM1 and

ΔRRM2 TDP-43 were co-expressed (Fig. 5, H, L, and P). Therefore, the data suggest that RRM1 and RRM2 play different or even opposing functions in the assembly of TDP-43 NBs, possibly by interacting with different RNAs and other RNA-binding NB proteins via the different RRMs.

RNA suppresses TDP-43 *in vitro* de-mixing via the RRMs

Recent studies indicate that the de-mixing process by LLPS condenses RBPs into LD-like compartments, allowing for the formation of intracellular membraneless RNP granules (*25*-*29*). Several ALS-related RBPs including TDP-43, FUS, hnRNP A1, hnRNP A2 and TIA1 have been shown to phase separate *in vitro* (*14*, *30*-*35*). The dynamic, reversible and membraneless characteristics of TDP-43 NBs suggested that LLPS might be involved in the formation of TDP-43 NBs. Indeed, we found that purified full-length (FL) TDP-43 underwent LLPS and formed LDs *in vitro* in a dose-dependent manner (Fig. S6, A to C). Similar to the observation in cells (Fig. S5, G and G'), the C-terminal LCD truncation (TDP-43$^{1\text{-}274}$) showed greatly reduced LLPS capability (Fig. S6D), suggesting a major role of the LCD in mediating TDP-43 de-mixing *in vitro* and *in vivo*. Nevertheless, the formation of TDP-43$^{1\text{-}274}$ LDs was evident at a higher protein concentration (50 μM) (Fig. S6D), confirming the previous observation that the N-terminal domains of TDP-43 could drive LLPS *in vivo* (*32*).

To gain insights into the mechanism involved in the regulation of TDP-43 NBs, we determined how RNA impacts on the LLPS of TDP-43 by adding total RNAs extracted from HeLa cells into the *in vitro* de-mixing system (Fig. S6, E and F). The addition of total RNAs markedly reduced the LLPS of FL TDP-43 at a concentration of 500 ng/μl (Fig. S6E), whereas a much lower concentration of total RNAs (100 ng/μl) was sufficient to suppress the LLPS of TDP-43$^{1\text{-}274}$ (Fig. S6F). These results confirm the predominant LLPS-promoting role of the C-terminal LCD and suggest an LLPS-suppressing function for the N-terminal RNA-binding regions. We then moved on to test how the two RRMs were involved in the RNA suppression of TDP-43 LLPS. Since the LLPS-promoting effect of the LCD in TDP-43 was overwhelming and made the function of the RRMs in RNA suppression difficult to assess in the *in vitro* de-mixing assay (Fig. S6, E and

F), we instead generated and tested ΔRRM1 and ΔRRM2 TDP-43$^{1-274}$ proteins (Fig. 6A and Fig. S6G). We confirmed that the RNA-binding affinity of ΔRRM1 and ΔRRM2 TDP-43$^{1-274}$ was significantly reduced (Fig. S6, H and I). WT as well as ΔRRM1 and ΔRRM2 TDP-43$^{1-274}$ formed LDs by LLPS *in vitro* in a dose-dependent manner, though the de-mixing of ΔRRM1 TDP-43$^{1-274}$ appeared less robust than that of WT or ΔRRM2 (Fig. S6, J to L).

To better compare the difference in RNA suppression, we lowered the NaCl concentration and increased the crowding agent PEG, which allowed WT TDP-43$^{1-274}$ to form larger LDs (Fig. 6B). We found that total RNAs at a concentration of 100 ng/μl markedly reduced the size and number of LDs of WT TDP-43$^{1-274}$. ΔRRM1 TDP-43$^{1-274}$ did not form large LDs as WT at the concentration of 50 μM and we initially thought its LLPS would be more easily suppressed by total RNAs. To our surprise, a much higher concentration (500 ng/μl) of total RNAs was required to see effective suppression (Fig. 6C), suggesting that deletion of the RRM1 greatly reduced the ability of total RNAs to suppress the formation of TDP-43 droplets, which was consistent with the finding that ΔRRM1 TDP-43 spontaneously phase separated into ring-like nuclear structures in cells even in the absence of cellular stress (Fig. S5H). We also tested ΔRRM1 TDP-43$^{1-274}$ at 100 μM to allow large ΔRRM1 LDs to form and the result confirmed that the suppression of TDP-43 LLPS by total RNAs was dramatically reduced with ΔRRM1, requiring total RNAs of about 250 ng/μl (Fig. 6C'). The suppression of the LLPS of ΔRRM2 TDP-43$^{1-274}$ by total RNAs (100~250 ng/μl) was slightly reduced compared to that of WT (Fig. 6, B and D), but to a less extent than that of ΔRRM1 (Fig. 6, C and C'). It was worth noting that ΔRRM1 TDP-43$^{1-274}$ showed both decreased LLPS capacity and reduced sensitivity to RNA suppression, indicating that a RBP with a lower tendency to phase separate on its own does not necessarily makes its LLPS more sensitive to RNA suppression. Nevertheless, these data indicate that both RRMs are involved in RNA suppression of TDP-43 LLPS.

Upregulation of *NEAT1* RNA promotes TDP-43 LLPS

Recent works have revealed both positive and negative regulation of LLPS of prion-like

RBPs by RNA (*62*). For example, tRNA was shown to reduce the LLPS of FUS *in vitro* (*50*). Similarly, tRNA also potently suppressed the *in vitro* LLPS of TDP-43 (Fig. 6E). We further examined the function of the two RRMs in mediating tRNA suppression. We found that ΔRRM1 TDP-43$^{1-274}$ showed similar sensitivity to tRNA suppression, as 1.25 μg/μl of tRNA was sufficient to suppress the LLPS of both WT and ΔRRM1 TDP-43$^{1-274}$ (Fig. 6, E and F). At this condition, however, ΔRRM2 LDs could still be observed and the effective suppression required a higher concentration of tRNA (2.5 μg/μl). It should be pointed out that, unlike the response to total RNAs, ΔRRM1 TDP-43$^{1-274}$ did not exhibit a greatly decreased sensitivity to tRNA suppression, despite that again only small ΔRRM1 LDs were present at the beginning of the suppression test. Thus, the lack of a strong suppression of ΔRRM1 LLPS by total RNAs (Fig. 6C) was not simply because suppression of small LDs was difficult to detect.

Since stress-induced TDP-43 NBs were co-localized with paraspeckles (Fig. S1, A and B) and TDP-43 bound directly to the paraspeckle scaffolding RNA *NEAT1* (*18*, *63*), we next examined whether *NEAT1* RNA impacted on the phase behavior of TDP-43. Interestingly, we found that *NEAT1* promoted the LLPS of TDP-43 in a dose-dependent manner (Fig. 6H), and this regulation by *NEAT1* required both the RRM1 and RRM2 of TDP-43 (Fig. 6, I and J). Furthermore, we showed that increasing concentrations of *NEAT1* antagonized the suppressing effect of tRNA, inducing the formation of TDP-43 droplets *in vitro* (Fig. 6K). In this suppressive environment, the *NEAT1*-mediated induction of the LLPS of ΔRRM1 TDP-43$^{1-274}$ was markedly reduced (Fig. 6L), which was consistent with the observations that ΔRRM1 TDP-43 remained soluble and LMB did not promote the formation of NBs or increase the number of the ring-like nuclear structures in cells (Fig. S5, D, H and H'). Under the same condition, *NEAT1* RNA more readily induced the *in vitro* de-mixing of ΔRRM2 TDP-43$^{1-274}$ (Fig. 6M), likely because tRNA suppression of ΔRRM2 was less effective (Fig. 6G). The overall increased tendency to form LDs and to remain phase separated might underlie the formation of more condensed, insoluble TDP-43 NBs by ΔRRM2 (Fig. S5, E, I and I').

Given that *NEAT1* RNA could act as scaffolds to promote the nucleation of paraspeckles (*50*, *64*-*67*) and that stress-induced TDP-43 NBs were partially co-localized with paraspeckles (Fig. S1, A and B), our data strongly suggest that *NEAT1* plays an important role in triggering the formation of stress-induced TDP-43 NBs in cells. Supporting this hypothesis, we found that the levels of both the total *NEAT1* RNA and the long non-coding RNA (lncRNA) isoform *NEAT1_2* were dramatically increased in mouse primary neurons treated with arsenite (Fig. 6N) or LMB (Fig. 6O), consistent with the observation earlier in this study that TDP-43 formed NBs in stressed neurons (Fig. S2, C and D). Together, we propose that cellular stress increases NEAT1 RNA levels, which antagonize the suppressive environment of the nucleoplasm by providing nucleation scaffolds that condensate TDP-43 and other NB components, triggering the formation of TDP-43 NBs in stressed cells.

ALS-associated D169G mutation of TDP-43 shows a specific defect in NB formation

This study was launched by the discovery that TDP-43 formed cytotoxicity-antagonizing NBs in mammalian cells and the formation of NBs alleviated TDP-43-mediated neurodegeneration in flies. To further investigate the relevance of TDP-43 NBs in the pathogenesis of human diseases, we examined several known ALS-causing TDP-43 mutants. Interestingly, we found that the mutation of D169G (640A>T) (*4*; and Fig. 7A) dramatically reduced the capability of TDP-43 to form NBs in response to stress induced by arsenite (Fig. 7, B to D) or LMB (Fig. S7, A to C). In contrast, the nucleocytoplasmic transport and recruitment of D169G TDP-43-D169G to SGs was unaffected (Fig. 7, B and E), which was consistent with the previous assessments of D169G in SG formation (*68*, *69*). The D169G mutation is in the RRM1, which is thought to cause a local conformational change that increases the thermal stability of the RRM1 (*70*, *71*). It is worth noting that most known disease-associated mutations such as M337V are enriched in the LCD region of TDP-43 (Fig. S7, D and E), which are thought to promote aberrant phase transition of SGs to irreversible protein aggregates in disease (*11*). Unlike D169G, we did not observe a significant effect of M337V mutation on the assembly of TDP-43 NBs (Fig. S7, F and G). Thus,

TDP-43^{D169G} has a specific defect in the formation of stress-induced NBs. In addition, these findings indicate that although TDP-43 NBs and SGs are both phase-separated RNP granules, the exact mechanisms regulating their assembly are different.

Next, we examined if the phase separation behavior of TDP-43-D169G was altered, which might contribute to the defect in TDP-43 NB formation. We found that purified D169G TDP-43$^{1-274}$ protein formed LDs in a dose-dependent manner just like that of WT in the *in vitro* LLPS assay (Fig. 7, F, G and H), suggesting that the ability of D169G to phase separate was not dramatically changed. Further, the suppression of TDP-43 LLPS by total RNAs showed no difference in D169G compared to that of WT TDP-43$^{1-274}$ (Fig. 7, I and J), suggesting the normal regulation of TDP-43 RNP granules by total RNAs remained intact in D169G. This was consistent with the result that D169G did not affect SG assembly or TDP-43 translocation to SGs (Fig. 7B and 7E). In striking contrast, the induction of TDP-43 LLPS by *NEAT1* RNA was drastically reduced in D169G (Fig. 7, K and L). Thus, these data not only well cohered with the observation that TDP-43-D169G was defective in NB formation but also further confirmed the crucial role of *NEAT1* in triggering the assembly of TDP-43 NBs. Together with the cytotoxicity-antagonizing function of TDP-43 NBs (Fig. 3 and Fig. 4), the findings of D169G (Fig. 7) suggest that a compromise of stress-induced TDP-43 NBs may be involved in ALS pathogenesis.

DISCUSSION

This study was initiated by the finding that TDP-43 formed distinct nuclear granules in stressed cells. We then characterized these subnuclear structures and demonstrated that they meet the three criteria of NBs (*15*) – (1) microscopically distinctive; (2) enriched of TDP-43 and partially colocalized with paraspeckles; and (3) liquid or hydrogel-like, highly dynamic and sensitive to the surrounding nucleoplasm. Further, we show that various cellular stresses such as arsenic stress, nuclear export blockage and proteasomal inhibition induce the formation of TDP-43 NBs. And TDP-43 NBs are detected in human cells, mouse primary neurons, and fly brains *in vivo*. Thus, the assembly of TDP-43 NBs may be a general stress response that occurs in multiple cell types and different organisms.

The cytotoxicity-antagonizing effect of TDP-43 NBs

Although TDP-43 insoluble aggregates are found in the nucleus and cytoplasm of affected neurons in ALS and FTD patients, reducing TDP-43 aggregates did not reduce or prevent cell death (*72*), suggesting that TDP-43 aggregation is associated with rather than a primary cause of neurodegeneration. Interestingly, we find in this study that NB-forming TDP-43 such as the NES^{mut} and the K145/192Q mutation are much less cytotoxic than diffused WT TDP-43. More importantly, abolishing the capability of TDP-43-NES^{mut} to form NBs makes the originally non-toxic NES^{mut} exhibit cytotoxicity. Furthermore, transgenic flies expressing TDP-43-NES^{mut} form remarkable NBs in the fly neurons and the neurodegeneration is considerably less severe than that of the TDP-43-WT flies. In line of the cytoprotective role, $TDP\text{-}43^{+}$ paraspeckles are observed in the spinal motor neurons of ALS patients especially in the early phases of the disease (*18*), suggesting that TDP-43 NBs may be called up and engaged in the first line of defense against cellular stress and disease conditions.

Paraspeckles are a class of subnuclear RNP granules formed by the scaffolding lncRNA *NEAT1* associated with SFPQ and other paraspeckle proteins (*64*, *66*, *73-75*), which are engaged in regulating different cellular functions through nuclear retention of specific mRNAs

and proteins (*76*-*78*). SGs sequester mRNAs and temporarily arrest protein synthesis to help cells survive stress (*79*). Given that TDP-43 is presented in both paraspeckles and SGs and plays an important role in regulating gene expression and RNA metabolism (*63*, *80*-*82*), it is reasonable to speculate that a similar underpinning mechanism may contribute to the cytoprotective function of TDP-43 NBs. For example, assembly of TDP-43 NBs may stall DNA transcription and/or arrest RNA processing; when stress is relieved, TDP-43 NBs disassemble and release the RNAs and nuclear proteins required for normal cell functions. In addition, since intranuclear inclusions of TDP-43 are also found in ALS patients (*83*), our data do not exclude the possibility that TDP-43 NBs may become irreversible protein aggregates under extended stress or diseased conditions.

The architecture of TDP-43 NBs and the functions of the two RRMs

The super-resolution 3D rendering reveals that TDP-43 NBs are ovals or cylinders in the nucleus rather than perfect spheres as inferred from the 2D images. The “roundness” has been described as one of the basic features for the notion that RNP granules are membraneless, intracellular compartments formed by LCD-mediated phase separation. Our data suggests that substantial additional forces, possibly provided by protein-protein and/or protein-RNA interactions, participate in assembling and shaping RNP granules, at least for the case of TDP-43 NBs.

TDP-43 contains two canonical RRMs in tandem. RRM1 has a longer Loop3 region than RRM2 and is thought to have a higher affinity for RNA targets (*84*-*85*). Although we did not detect a significant difference in the binding affinity between ΔRRM1 and ΔRRM2 to total RNAs in the dot-blot assay, they do show divergent sensitivities to RNA suppression in the *in vitro* LLPS assays, likely because that the two RRMs have different RNA preferences (*84*). It needs to be noted that the effects of RNA on ΔRRM1 and ΔRRM2 TDP-43 were compared without the LCD in the *in vitro* LLPS assays. This is because the LCD presents an overwhelming LLPS-driving force (*25*, *31*, *37*, *61*), whereas the *in vitro* LLPS system appears to be much less suppressive than the conditions in the nucleoplasm (see below).

In cells, TDP-43 is diffused in the nucleus and does not form NBs spontaneously under normal conditions. And, the partition of TDP-43 into phase-separated intracellular compartments requires the LCD (*31*, *61*, and also see Fig. S5). Thus, ΔRRM1 and ΔRRM2 are examined inclusive of the LCD in cell-based experiments in this study. ΔRRM1 lacks the RRM1-mediated suppression but contains the forceful LLPS-promoting LCD, which leads to spontaneous phase separation of ΔRRM1 in the nucleus. Meanwhile, since the RRM1 is also used by TDP-43 to anchor itself to the core of the NBs, the phase-separated ΔRRM1 forms large, ring-like structures. The seemingly conflicting effects of RRM1 – inhibiting TDP-43 phase separation under normal conditions whereas pushing TDP-43 toward the core of the NBs when the LLPS occurs – may be achieved by interacting with different RNAs. In contrast, since ΔRRM2 retains the main RNA suppression force mediated by RRM1, it does not spontaneously phase separate in the nucleus. When stressed, ΔRRM2 forms small, condensed NBs possibly because the RRM2-mediated "centrifugal force" is no longer available to counteract the RRM1-mediated "centripetal force". Together, we propose a "push-and-pull" model for the opposing effects of the two RRMs in maintaining the "core-shell" architecture of TDP-43 NBs.

The role of RNAs in regulating TDP-43 LDs and NBs

RNA can either promote or suppress the assembly of RNP granules depending on the concentrations and the types of the RNA (15, 16, *25*, *26*). In addition, the ALS/FTD-related C9ORF72 repeat RNA promotes phase transition and assembly of RNP granules in cells (*86*). In this study, we show that tRNA suppresses TDP-43 LLPS, similar to the effect on FUS (*50*); however, tRNA was previously shown to enhance Tau LLPS (*87*). Thus, even for the same RNA, its role may vary depending on the protein that it interacts with.

lncRNAs are thought to provide the scaffold for the assembly of paraspeckles (*64*, *65*, *67*) and nuclear stress bodies (*88*, *89*). In particular, the paraspeckle lncRNA *NEAT1* are increased in patients and/or animal models of several neurodegenerative diseases including ALS (*18*), Alzheimer's disease (*90*), Parkinson's disease (*91*), Huntington's disease (*92*), and multiple

sclerosis (*93*). In this study, we find that *NEAT1* lncRNA is substantially upregulated in stressed neurons and TDP-43 NBs are partially colocalized with paraspeckles, cohering with the similar observations in the spinal motor neurons of early ALS patients (*18*). Further *in vitro* experiments indicate that *NEAT1* RNA not only promotes TDP-43 LLPS, but also antagonizes the generally "suppressive" environment modeled using tRNA. Thus, stress-induced upregulation of *NEAT1* may provide nucleation scaffolds to concentrate TDP-43 and other NB proteins, which overturns the suppressive environment in the nucleoplasm, leading to the emergence of TDP-43 NBs. It is worth noting that lncRNAs are potential targets of TDP-43 (*94*-*96*), implying complicated cross-regulation between TDP-43 and *NEAT1* in this cellular stress response mechanism.

The D169G mutation and the relevance of TDP-43 NBs in ALS pathogenesis

More than 30 disease-causing mutations have been identified in the gene encoding TDP-43, of which most are in the LCD and the adjacent regions (*5*, *97*). D169G is the only known ALS-causing mutation within the RRM of TDP-43 (*4*) and its pathogenic mechanism has been elusive. Initially, it was presumed to abrogate RNA binding due to its location within the RRM (*4*). However, subsequent work indicates that the binding affinity of D169G to RNA or DNA is not decreased (*85*). And, although TDP-43^{D169G} exhibits slightly increased thermal stability and may be more susceptible to proteolytic cleavage (*70*, *71*), it does not engender aberrant oligomerization but rather increases the resistance of TDP-43 to aggregation (*70*). Further, the D169G mutation does not affect TDP-43 subcellular distribution or SG recruitment (*68*, *69*; also see Fig. 7). The only reported cellular alteration by D169G is that it reduces polyubiquitination and co-aggregation of TDP-43 with Ubiquilin 1 (98). However, given the long-standing notion that ubiquitinated cytoplasmic inclusions containing TDP-43 is a hallmark and major cause of the disease (*6*, *10*, *11*), it is difficult to understand how decreased ubiquitination and aggregation of TDP-43^{D169G} leads to disease pathogenesis.

In this study, we discover that TDP-43^{D169G} has a striking and specific defect in the formation of stress-induced TDP-43 NBs but not SGs. D169G is thought to cause a small local

conformational change in the Turn6 of the β-sheets within the RRM1 of TDP-43 (*70*, *71*), but does not reduce the overall binding affinity of TDP-43 to nucleic acids (*85*). Indeed, we find that the suppression of TDP-43 LLPS by total RNAs is unaffected by D169G, whereas the induction of TDP-43 LLPS by *NEAT1* is dramatically diminished. Together with the cytoprotective role of TDP-43 NBs, D169G provides a paradigm for compromise of TDP-43 NBs involved in ALS pathogenesis. Given that cytoplasmic mislocalization and nuclear depletion of TDP-43 are common in diseased neurons, it is likely that loss of the TDP-43 NB-mediated stress-mitigating function may also underlie other cases of ALS and related diseases.

519 **REFERENCES AND NOTES**

520 1. J. P. Taylor, R. H. Brown, Jr., D. W. Cleveland, Decoding ALS: from genes to mechanism.
521 *Nature* **539**, 197-206 (2016).

522 2. M. A. van Es *et al*., Amyotrophic lateral sclerosis. *The Lancet* **390**, 2084-2098 (2017).

523 3. M. Neumann *et al*., Ubiquitinated TDP-43 in frontotemporal lobar degeneration and
524 amyotrophic lateral sclerosis. *Science* **314**, 130-133 (2006).

525 4. E. Kabashi *et al*., TARDBP mutations in individuals with sporadic and familial amyotrophic
526 lateral sclerosis. *Nat Genet* **40**, 572-574 (2008).

527 5. E. B. Lee, V. M. Lee, J. Q. Trojanowski, Gains or losses: molecular mechanisms of
528 TDP43-mediated neurodegeneration. *Nat Rev Neurosci* **13**, 38-50 (2011).

529 6. A. Jovicic, J. W. Paul, 3rd, A. D. Gitler, Nuclear transport dysfunction: a common theme in
530 amyotrophic lateral sclerosis and frontotemporal dementia. *J Neurochem* **138 Suppl 1**,
531 134-144 (2016).

532 7. A. Ratti, E. Buratti, Physiological functions and pathobiology of TDP-43 and FUS/TLS
533 proteins. *J Neurochem* **138 Suppl 1**, 95-111 (2016).

534 8. H. Ederle, D. Dormann, TDP-43 and FUS en route from the nucleus to the cytoplasm. *FEBS*
535 *Letters* **591**, 1489-1507 (2017).

536 9. B. Fahrenkrog, A. Harel, Perturbations in Traffic: Aberrant Nucleocytoplasmic Transport at
537 the Heart of Neurodegeneration. *Cells* **7**, 232 (2018).

538 10. M. Zhao, J. R. Kim, R. van Bruggen, J. Park, RNA-Binding Proteins in Amyotrophic Lateral
539 Sclerosis. *Mol Cells* **41**, 818-829 (2018).

540 11. Y. R. Li, O. D. King, J. Shorter, A. D. Gitler, Stress granules as crucibles of ALS
541 pathogenesis. *J Cell Biol* **201**, 361-372 (2013).

542 12. M. Ramaswami, J. P. Taylor, R. Parker, Altered ribostasis: RNA-protein granules in
543 degenerative disorders. *Cell* **154**, 727-736 (2013).

544 13. T. Murakami *et al*., ALS/FTD Mutation-Induced Phase Transition of FUS Liquid Droplets and
545 Reversible Hydrogels into Irreversible Hydrogels Impairs RNP Granule Function. *Neuron* **88**,
546 678-690 (2015).

547 14. A. Patel *et al*., A Liquid-to-Solid Phase Transition of the ALS Protein FUS Accelerated by
548 Disease Mutation. *Cell* **162**, 1066-1077 (2015).

549 15. D. Stanek, A. H. Fox, Nuclear bodies: news insights into structure and function. *Curr Opin*
550 *Cell Biol* **46**, 94-101 (2017).

551 16. M. Wegener, M. Muller-McNicoll, Nuclear retention of mRNAs - quality control, gene
552 regulation and human disease. *Semin Cell Dev Biol* **79**, 131-142 (2018).

17. E. B. Dammer *et al*., Coaggregation of RNA-binding proteins in a model of TDP-43 proteinopathy with selective RGG motif methylation and a role for RRM1 ubiquitination. *PLoS One* **7**, e38658 (2012).

18. Y. Nishimoto *et al*., The long non-coding RNA nuclear-enriched abundant transcript 1_2 induces paraspeckle formation in the motor neuron during the early phase of amyotrophic lateral sclerosis. *Mol Brain* **6**, 31 (2013).

19. J. A. West *et al*., Structural, super-resolution microscopy analysis of paraspeckle nuclear body organization. *J Cell Biol* **214**, 817-830 (2016).

20. T. Ishihara *et al*., Decreased number of Gemini of coiled bodies and U12 snRNA level in amyotrophic lateral sclerosis. *Hum Mol Genet* **22**, 4136-4147 (2013).

21. M. Udan-Johns *et al*., Prion-like nuclear aggregation of TDP-43 during heat shock is regulated by HSP40/70 chaperones. *Hum Mol Genet* **23**, 157-170 (2014).

22. S. Lee *et al*., Identification of a subnuclear body involved in sequence-specific cytokine RNA processing. *Nat Commun* **6**, 5791 (2015).

23. L. Lo Piccolo *et al*., Loss of ISWI Function in Drosophila Nuclear Bodies Drives Cytoplasmic Redistribution of Drosophila TDP-43. *Int J Mol Sci* **19**, 1082 (2018).

24. H. An *et al*., ALS-linked FUS mutations confer loss and gain of function in the nucleus by promoting excessive formation of dysfunctional paraspeckles. *Acta Neuropathol Commun* **7**, 7 (2019).

25. Y. Lin, D. S. Protter, M. K. Rosen, R. Parker, Formation and Maturation of Phase-Separated Liquid Droplets by RNA-Binding Proteins. *Mol Cell* **60**, 208-219 (2015).

26. M. Feric *et al*., Coexisting Liquid Phases Underlie Nucleolar Subcompartments. *Cell* **165**, 1686-1697 (2016).

27. S. F. Banani, H. O. Lee, A. A. Hyman, M. K. Rosen, Biomolecular condensates: organizers of cellular biochemistry. *Nat Rev Mol Cell Biol* **18**, 285-298 (2017).

28. V. N. Uversky, Intrinsically disordered proteins in overcrowded milieu: Membrane-less organelles, phase separation, and intrinsic disorder. *Curr Opin Struct Biol* **44**, 18-30 (2017).

29. S. Nakagawa, T. Yamazaki, T. Hirose, Molecular dissection of nuclear paraspeckles: towards understanding the emerging world of the RNP milieu. *Open Biol* **8**, pii: 180150 (2018).

30. A. A. Hyman, C. A. Weber, F. Julicher, Liquid-liquid phase separation in biology. *Annu Rev Cell Dev Biol* **30**, 39-58 (2014).

31. A. Molliex *et al*., Phase separation by low complexity domains promotes stress granule assembly and drives pathological fibrillization. *Cell* **163**, 123-133 (2015).

32. H. B. Schmidt, R. Rohatgi, In Vivo Formation of Vacuolated Multi-phase Compartments

588 Lacking Membranes. *Cell Rep* **16**, 1228-1236 (2016).

589 33. I. R. Mackenzie *et al*., TIA1 Mutations in Amyotrophic Lateral Sclerosis and Frontotemporal
590 Dementia Promote Phase Separation and Alter Stress Granule Dynamics. *Neuron* **95**,
591 808-816.e809 (2017).

592 34. V. H. Ryan *et al*., Mechanistic View of hnRNPA2 Low-Complexity Domain Structure,
593 Interactions, and Phase Separation Altered by Mutation and Arginine Methylation. *Molecular*
594 *Cell* **69**, 465-479.e467 (2018).

595 35. L. Wang, J. Kang, L. Lim, Y. Wei, J. Song, TDP-43 NTD can be induced while CTD is
596 significantly enhanced by ssDNA to undergo liquid-liquid phase separation. *Biochem*
597 *Biophys Res Commun* **499**, 189-195 (2018).

598 36. S. Hennig *et al*., Prion-like domains in RNA binding proteins are essential for building
599 subnuclear paraspeckles. *J Cell Biol* **210**, 529-539 (2015).

600 37. S. Xiang *et al*., The LC Domain of hnRNPA2 Adopts Similar Conformations in Hydrogel
601 Polymers, Liquid-like Droplets, and Nuclei. *Cell* **163**, 829-839 (2015).

602 38. D. T. Murray *et al*., Structure of FUS Protein Fibrils and Its Relevance to Self-Assembly and
603 Phase Separation of Low-Complexity Domains. *Cell* **171**, 615-627 e616 (2017).

604 39. O. A. Brady, P. Meng, Y. Zheng, Y. Mao, F. Hu, Regulation of TDP-43 aggregation by
605 phosphorylation and p62/SQSTM1. *J Neurochem* **116**, 248-259 (2011).

606 40. T. J. Cohen *et al*., An acetylation switch controls TDP-43 function and aggregation
607 propensity. *Nat Commun* **6**, 5845 (2015).

608 41. W. Li *et al*., Heat Shock-induced Phosphorylation of TAR DNA-binding Protein 43 (TDP-43)
609 by MAPK/ERK Kinase Regulates TDP-43 Function. *J Biol Chem* **292**, 5089-5100 (2017).

610 42. M. Hofweber *et al*., Phase Separation of FUS Is Suppressed by Its Nuclear Import Receptor
611 and Arginine Methylation. *Cell* **173**, 706-719.e713 (2018).

612 43. F. Luo *et al*., Atomic structures of FUS LC domain segments reveal bases for reversible
613 amyloid fibril formation. *Nat Struct Mol Biol* **25**, 341-346 (2018).

614 44. L. McGurk *et al*., Poly(ADP-Ribose) Prevents Pathological Phase Separation of TDP-43 by
615 Promoting Liquid Demixing and Stress Granule Localization. Molecular *Cell* **71**,
616 703-717.e709 (2018).

617 45. S. Qamar *et al*., FUS Phase Separation Is Modulated by a Molecular Chaperone and
618 Methylation of Arginine Cation-pi Interactions. *Cell* **173**, 720-734 e715 (2018).

619 46. Y. Duan *et al*., PARylation regulates stress granule dynamics, phase separation, and
620 neurotoxicity of disease-related RNA-binding proteins. *Cell Res* **29**, 233-247 (2019).

621 47. D. Dominguez *et al*., Sequence, Structure, and Context Preferences of Human RNA Binding
622 Proteins. *Mol Cell* **70**, 854-867 e859 (2018).

623 48. S. Namkoong, A. Ho, Y. M. Woo, H. Kwak, J. H. Lee, Systematic Characterization of
624 Stress-Induced RNA Granulation. *Mol Cell* **70**, 175-187 e178 (2018).

625 49. S. P. Shevtsov, M. Dundr, Nucleation of nuclear bodies by RNA. *Nat Cell Biol* **13**, 167-173
626 (2011).

627 50. S. Maharana *et al.*, RNA buffers the phase separation behavior of prion-like RNA binding
628 proteins. *Science* **360**, 918-921 (2018).

629 51. J. R. Mann *et al.*, RNA Binding Antagonizes Neurotoxic Phase Transitions of TDP-43.
630 *Neuron* **102**, 1-18 (2019).

631 52. L. Bernstam, J. Nriagu, Molecular aspects of arsenic stress. *J Toxicol Environ Health B Crit*
632 *Rev* **3**, 293-322 (2000).

633 53. L. A. Kominek, Cycloheximide Production by Streptomyces griseus Control Mechanisms of
634 Cycloheximide Biosynthesis. *Antimicrob Agents Chemother* **7**, 856-860 (1975).

635 54. F. Frottin *et al.*, The nucleolus functions as a phase-separated protein quality control
636 compartment. *Science* **365**, 342-347 (2019).

637 55. D. Glick, S. Barth, K. F. Macleod, Autophagy: cellular and molecular mechanisms. *J Pathol*
638 **221**, 3-12 (2010).

639 56. S. J. Barmada *et al.*, Autophagy induction enhances TDP43 turnover and survival in
640 neuronal ALS models. *Nature Chemical Biology* **10**, 677-685 (2014).

641 57. A. H. Brand, N. Perrimon, Targeted gene expression as a means of altering cell fates and
642 generating dominant phenotypes. *Development* **118**, 401-415 (1993).

643 58. A. C. Groth, M. Fish, R. Nusse, M. P. Calos, Construction of transgenic Drosophila by using
644 the site-specific integrase from phage PhiC31. *Genetics* **166**, 1775-1782 (2003).

645 59. J. R. Bateman, A. M. Lee, C. T. Wu, Site-specific transformation of Drosophila via phiC31
646 integrase-mediated cassette exchange. *Genetics* **173**, 769-777 (2006).

647 60. J. Bischof, R. K. Maeda, M. Hediger, F. Karch, K. Basler, An optimized transgenesis system
648 for Drosophila using germ-line-specific phiC31 integrases. *Proc Natl Acad Sci U S A* **104**,
649 3312-3317 (2007).

650 61. A. E. Conicella, G. H. Zerze, J. Mittal, N. L. Fawzi, ALS Mutations Disrupt Phase Separation
651 Mediated by alpha-Helical Structure in the TDP-43 Low-Complexity C-Terminal Domain.
652 *Structure* **24**, 1537-1549 (2016).

653 62. L. Guo, J. Shorter, It's Raining Liquids: RNA Tunes Viscoelasticity and Dynamics of
654 Membraneless Organelles. *Mol Cell* **60**, 189-192 (2015).

655 63. J. R. Tollervey *et al.*, Characterizing the RNA targets and position-dependent splicing
656 regulation by TDP-43. *Nat Neurosci* **14**, 452-458 (2011).

657 64. C. M. Clemson *et al.*, An architectural role for a nuclear noncoding RNA: NEAT1 RNA is

658 essential for the structure of paraspeckles. *Mol Cell* **33**, 717-726 (2009).

659 65. L. L. Chen, G. G. Carmichael, Altered nuclear retention of mRNAs containing inverted
660 repeats in human embryonic stem cells: functional role of a nuclear noncoding RNA. *Mol*
661 *Cell* **35**, 467-478 (2009).

662 66. Y. T. Sasaki, T. Ideue, M. Sano, T. Mituyama, T. Hirose, MENepsilon/beta noncoding RNAs
663 are essential for structural integrity of nuclear paraspeckles. *Proc Natl Acad Sci U S A* **106**,
664 2525-2530 (2009).

665 67. T. Yamazaki *et al*., Functional Domains of NEAT1 Architectural lncRNA Induce Paraspeckle
666 Assembly through Phase Separation. *Molecular Cell* **70**, 1038-1053.e1037 (2018).

667 68. K. K. McDonald *et al*., TAR DNA-binding protein 43 (TDP-43) regulates stress granule
668 dynamics via differential regulation of G3BP and TIA-1. *Hum Mol Genet* **20**, 1400-1410
669 (2011).

670 69. E. Bentmann *et al*., Requirements for stress granule recruitment of fused in sarcoma (FUS)
671 and TAR DNA-binding protein of 43 kDa (TDP-43). *J Biol Chem* **287**, 23079-23094 (2012).

672 70. J. A. Austin *et al*., Disease causing mutants of TDP-43 nucleic acid binding domains are
673 resistant to aggregation and have increased stability and half-life. *Proc Natl Acad Sci U S A*
674 **111**, 4309-4314 (2014).

675 71. C. H. Chiang *et al*., Structural analysis of disease-related TDP-43 D169G mutation: linking
676 enhanced stability and caspase cleavage efficiency to protein accumulation. *Sci Rep* **6**,
677 21581 (2016).

678 72. Y. C. Liu, P. M. Chiang, K. J. Tsai, Disease animal models of TDP-43 proteinopathy and
679 their pre-clinical applications. *Int J Mol Sci* **14**, 20079-20111 (2013).

680 73. A. H. Fox *et al*., Paraspeckles: A Novel Nuclear Domain. *Current Biology* **12**, 13-25 (2002)

681 74. K. V. Prasanth *et al*., Regulating gene expression through RNA nuclear retention. *Cell* **123**,
682 249-263 (2005).

683 75. T. Naganuma *et al*., Alternative 3'-end processing of long noncoding RNA initiates
684 construction of nuclear paraspeckles. *EMBO J* **31**, 4020-4034 (2012).

685 76. C. S. Bond, A. H. Fox, Paraspeckles: nuclear bodies built on long noncoding RNA. *J Cell*
686 *Biol* **186**, 637-644 (2009).

687 77. A. H. Fox, A. I. Lamond, Paraspeckles. *Cold Spring Harb Perspect Biol* **2**, a000687 (2010).

688 78. A. H. Fox, S. Nakagawa, T. Hirose, C. S. Bond, Paraspeckles: Where Long Noncoding RNA
689 Meets Phase Separation. *Trends Biochem Sci* **43**, 124-135 (2018).

690 79. L. Liu-Yesucevitz *et al*., Tar DNA binding protein-43 (TDP-43) associates with stress
691 granules: analysis of cultured cells and pathological brain tissue. *PLoS One* **5**, e13250
692 (2010).

80. J. K. Bose, I. F. Wang, L. Hung, W. Y. Tarn, C. K. Shen, TDP-43 overexpression enhances exon 7 inclusion during the survival of motor neuron pre-mRNA splicing. *J Biol Chem* **283**, 28852-28859 (2008).

81. T. W. Han *et al*., Cell-free formation of RNA granules: bound RNAs identify features and components of cellular assemblies. *Cell* **149**, 768-779 (2012).

82. J. Seo *et al*., Oxidative Stress Triggers Body-Wide Skipping of Multiple Exons of the Spinal Muscular Atrophy Gene. *PLoS One* **11**, e0154390 (2016).

83. M. S. Forman, J. Q. Trojanowski, V. M. Lee, TDP-43: a novel neurodegenerative proteinopathy. *Curr Opin Neurobiol* **17**, 548-555 (2007).

84. E. Buratti, F. E. Baralle, Characterization and functional implications of the RNA binding properties of nuclear factor TDP-43, a novel splicing regulator of CFTR exon 9. *J Biol Chem* **276**, 36337-36343 (2001).

85. P. H. Kuo, C. H. Chiang, Y. T. Wang, L. G. Doudeva, H. S. Yuan, The crystal structure of TDP-43 RRM1-DNA complex reveals the specific recognition for UG- and TG-rich nucleic acids. *Nucleic Acids Res* **42**, 4712-4722 (2014).

86. M. M. Fay, P. J. Anderson, P. Ivanov, ALS/FTD-Associated C9ORF72 Repeat RNA Promotes Phase Transitions In Vitro and in Cells. *Cell Rep* **21**, 3573-3584 (2017).

87. T. Ukmar-Godec *et al*., Lysine/RNA-interactions drive and regulate biomolecular condensation. *Nat Commun* **10**, 2909 (2019).

88. C. Jolly et al., Stress-induced transcription of satellite III repeats. *J Cell Biol* **164**, 25-33 (2004).

89. R. Valgardsdottir et al., Structural and Functional Characterization of Noncoding Repetitive RNAs Transcribed in Stressed Human Cells. *Molecular Biology of the Cell* **16**, 2597-2604 (2005).

90. N. Puthiyedth, C. Riveros, R. Berretta, P. Moscato, Identification of Differentially Expressed Genes through Integrated Study of Alzheimer's Disease Affected Brain Regions. *PLoS One* **11**, e0152342 (2016).

91. E. Mariani *et al*., Meta-Analysis of Parkinson's Disease Transcriptome Data Using TRAM Software: Whole Substantia Nigra Tissue and Single Dopamine Neuron Differential Gene Expression. *PLoS One* **11**, e0161567 (2016).

92. C. Cheng *et al*., The long non-coding RNA NEAT1 is elevated in polyglutamine repeat expansion diseases and protects from disease gene-dependent toxicities. *Hum Mol Genet* **27**, 4303-4314 (2018).

93. L. Schirmer *et al*., Neuronal vulnerability and multilineage diversity in multiple sclerosis. *Nature* [Epub ahead of print] (2019).

94. M. Polymenidou *et al*., Long pre-mRNA depletion and RNA missplicing contribute to

729 neuronal vulnerability from loss of TDP-43. *Nat Neurosci* **14**, 459-468 (2011).

730 95. C. Y. Chung *et al*., Aberrant activation of non-coding RNA targets of transcriptional
731 elongation complexes contributes to TDP-43 toxicity. *Nat Commun* **9**, 4406 (2018).

732 96. M. Modic *et al*., Cross-Regulation between TDP-43 and Paraspeckles Promotes
733 Pluripotency-Differentiation Transition. *Mol Cell* **74**, 951-965 e913 (2019).

734 97. A. S. Chen-Plotkin, V. M. Lee, J. Q. Trojanowski, TAR DNA-binding protein 43 in
735 neurodegenerative disease. *Nat Rev Neurol* **6**, 211-220 (2010).

736 98. S. H. Kim *et al*., Potentiation of amyotrophic lateral sclerosis (ALS)-associated TDP-43
737 aggregation by the proteasome-targeting factor, ubiquilin 1. *J Biol Chem* **284**, 8083-8092
738 (2009).

739 99. X. Sun *et al*., Distinct multilevel misregulations of Parkin and PINK1 revealed in cell and
740 animal models of TDP-43 proteinopathy. *Cell Death Dis* **9**, 953 (2018).

741 100. X. Cao *et al*., In vivo imaging reveals mitophagy independence in the maintenance of axonal
742 mitochondria during normal aging. *Aging Cell* **16**, 1180-1190 (2017).

743 101. M. H. M. Koken *et al*., The t(15;17) translocation alters a nuclear body in a retinoic
744 acid-reversible fashion. *The EMBO Journal* **13**, 1073-1083 (1994).

745 102. N. Santama *et al*., Characterization of hCINAP, a novel coilin-interacting protein encoded by
746 a transcript from the transcription factor TAFIID32 locus. *J Biol Chem* **280**, 36429-36441
747 (2005).

748 103. X-D. Fu, T. Maniatis, Factor required for mammalian spliceosome assembly is localized to
749 discrete regions in the nucleus. *Nature* **343**, 437–444 (1990).

ACKNOWLEDGMENTS

We thank the BDSC for providing the fly strains, the SIBCB *Drosophila* Center for the fly embryo injection services, L. Pan, J. Zhou, and Z. Zhang for the cloning vectors and plasmids, Z. Zhang for help in the pulse-chase assay, S. Qiu for technical supports, J. Yuan, A. Li and Y. Chen for critical reading of the manuscript, and the members of the Fang lab for helpful discussion. **Funding**: Supported by grants from the National Key R&D Program of China (No. 2016YFA0501902) to Y.F., the National Natural Science Foundation of China (No. 81671254 and No. 31471017) to Y.F and (No. 91853112 and No. 31470748) to C.L, and the Alzheimer's AssOCiation (AARF-16-441196) and Target ALS Springboard Fellowship to L.G. **Author contributions:** G.D., Z.M. and Y.F. conceived the research; C.W., Y.D., G.D., C.L., L.G. and Y.F. designed the experiments; C.W., Y.D. G.D., K.Z., X.D., B.Q., J.G. and S.Z. performed the experiments; C.W., Y.D., G.D., Z.M., J.G. and C.L contributed important new reagents; C.W., Y.D. G.D., and Y.F. analyzed the data and interpreted the results; C.W., Y.D., G.D. and Y.F. prepared the figures; and C.W., Y.D. G.D., and Y.F. wrote the paper. All authors read and approved the final manuscript. **Competing interests:** None. **Data and materials availability:** All data are available in the manuscript or the supplementary materials.

SUPPLEMENTARY INFORMATION

Online Methods

Figures S1-S7

Movies S1-S2

References (99-103)

772 **FIGURES AND FIGURE LEGENDS**

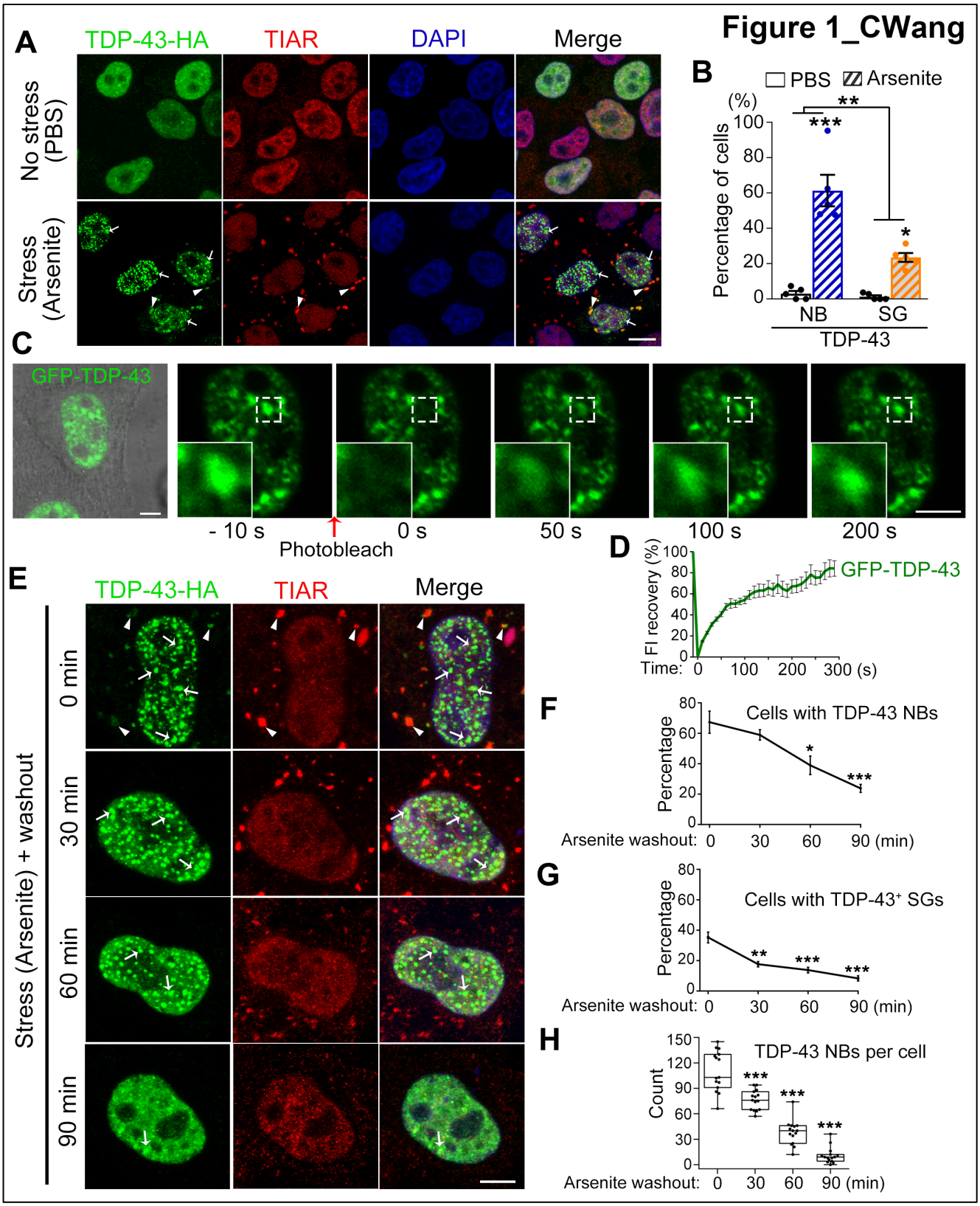

Figure 1. TDP-43 forms reversible, dynamic NBs in response to arsenic stress.

(**A**) Representative confocal images of HeLa cells in the absence (PBS) or presence of arsenite (250 μM, 30 min) forming TDP-43 NBs (arrows) and TDP-43$^+$ SGs (arrowheads) (also see Movie S1). All cells are transfected with TDP-43-HA (anti-HA) and stained for SGs with anti-TIAR; merged images with DAPI staining for DNA (blue) are shown. Arrows, TDP-43 NBs; arrowheads, SGs associated with TDP-43 (TDP-43$^+$ SGs). (**B**) Quantification of the percentage of cells that show TDP-43 NBs or TDP-43$^+$ SGs before and after arsenite the treatment in (A). Data are shown as mean ± SEM, n = ~100 cells for each group from pooled results of 3 independent repeats; *p < 0.05, **p < 0.01, ***p < 0.001; Student's t-test for comparison between stress and no stress within the same group, two-way ANOVA for comparison of the stress-induced changes between different groups. (**C**) Representative images of the FRAP analysis of GFP-TDP-43 NBs in *live* cells (also see Movie S2). (**D**) The FRAP recovery curve is quantified by averaging the relative fluorescence intensity (FI) of 9 TDP-43 NBs of similar size at indicated time after photobleaching. The relative FI of each TDP-43 NB prior to photobleaching is set to 100%. Time 0 refers to the time point right after photobleaching. (**E**) Representative images showing the disappearance of TDP-43 NBs and TDP-43$^+$ SGs after arsenite washout. (**F-H**) Quantification of the percentage of cells showing TDP-43 NBs (F), TDP-43$^+$ SGs (G) or the average count of TDP-43 NBs per cell (H) at indicated time points after arsenite washout in (E). Mean ± SEM, except for (H) box-and-whisker plots. n = ~100 cells for each group in (F-G) and ~15 cells for each group in (H), pooled results from 3 independent repeats; statistic significance is determined by comparing to time 0; *p < 0.05, **p < 0.01, ***p < 0.001; one-way ANOVA. Scale bars, 10 μm in (A) and 5 μm in (C, E).

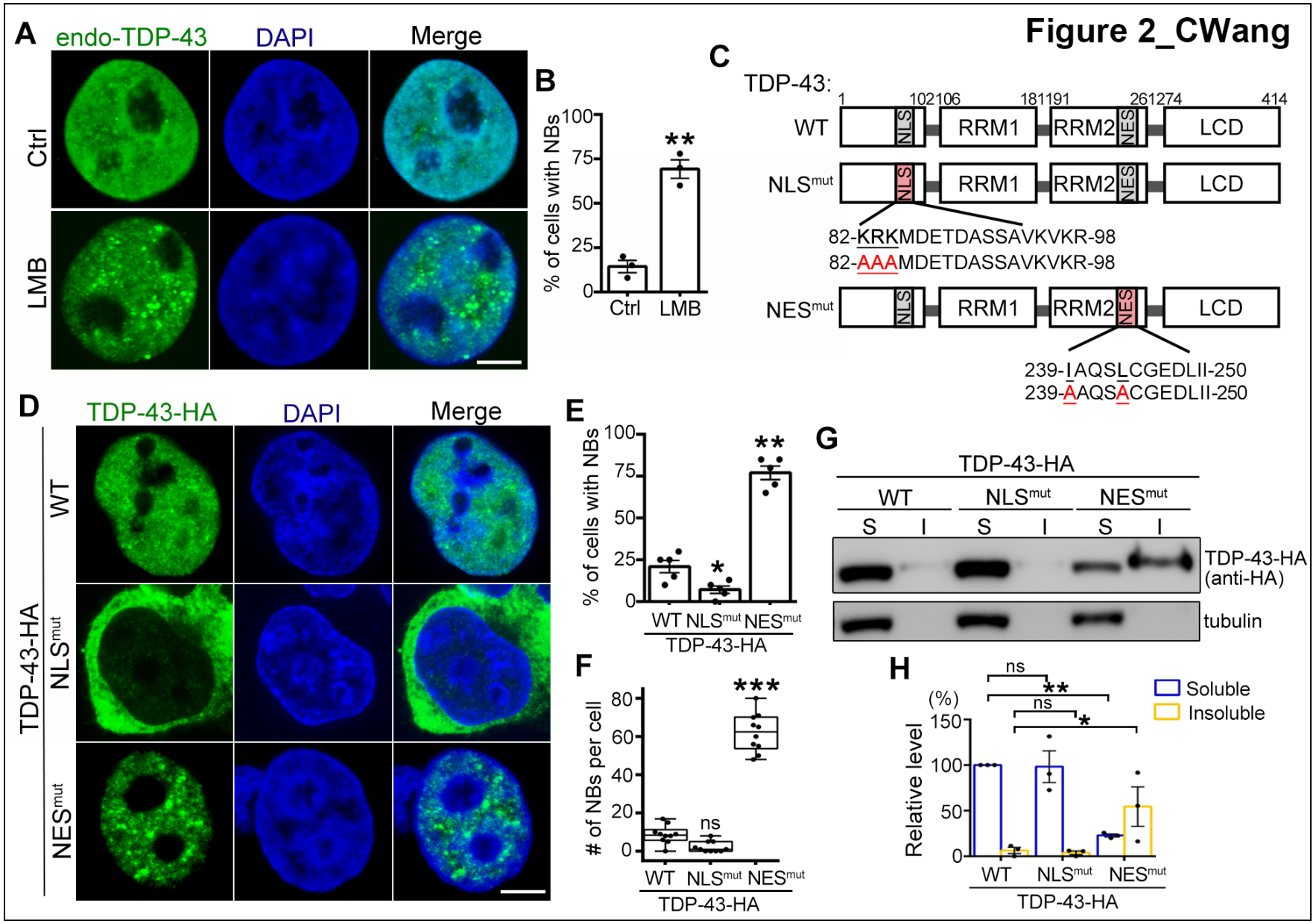
Figure 2_CWang
A
endo-TDP-43
DAPI
Merge
Ctrl
LMB
B
% of cells with NBs
Ctrl
LMB
C
TDP-43:
WT
NLSmut
NESmut
NLS
RRM1
RRM2
NES
LCD
82-KRKMDETDASSAVKVKR-98
82-AAAMDETDASSAVKVKR-98
239-IAQSLCGEDLII-250
239-AAQSACGEDLII-250
D
TDP-43-HA
DAPI
Merge
WT
NLSmut
NESmut
E
% of cells with NBs
WT NLSmut NESmut
TDP-43-HA
F
# of NBs per cell
ns
WT NLSmut NESmut
TDP-43-HA
G
TDP-43-HA
WT
NLSmut
NESmut
S
I
TDP-43-HA (anti-HA)
tubulin
H
(%)
ns
Soluble
Insoluble
Relative level
WT NLSmut NESmut
TDP-43-HA

796

Figure 2. Inhibition of nuclear export induces TDP-43 NBs.

(**A-B**) Representative images of endogenous TDP-43 (endo-TDP-43) forming NBs upon LMB treatment (25 nM, 24 h). Percentage of cells showing distinct TDP-43 NBs in (A) is quantified in (B). (**C**) A diagram showing the major domains of human TDP-43 and the residues mutated in the localization signals. NLS, nuclear localization signal; RRM, RNA recognition motif; NES, nuclear export signal; LCD, low complexity domain. (**D**) Representative images of 293T cells transfected with WT, NLS^{mut} or NES^{mut} TDP-43. (**E-F**) The percentage of cells with NBs (E) and the average number of NBs per cell (F) are quantified. (**G-H**) Representative Western blot images (G) and quantifications (H) of WT, NLS^{mut} and NES^{mut} TDP-43 proteins in the soluble (S, supernatants in RIPA) and insoluble fractions (I, pellets resuspended in 9 M of urea). Mean ± SEM, except for (F) box-and-whisker plots. n >120 cells each condition in (B, E) and ~ 10 cells each condition in (F) from pooled results of 3 independent repeats, n = 3 in (G-H); $*p < 0.05$, $**p < 0.01$, $***p < 0.001$; ns, not significant; Student's *t*-test in (B), one-way ANOVA in (E-F, H). Scale bar: 5 μm.

811

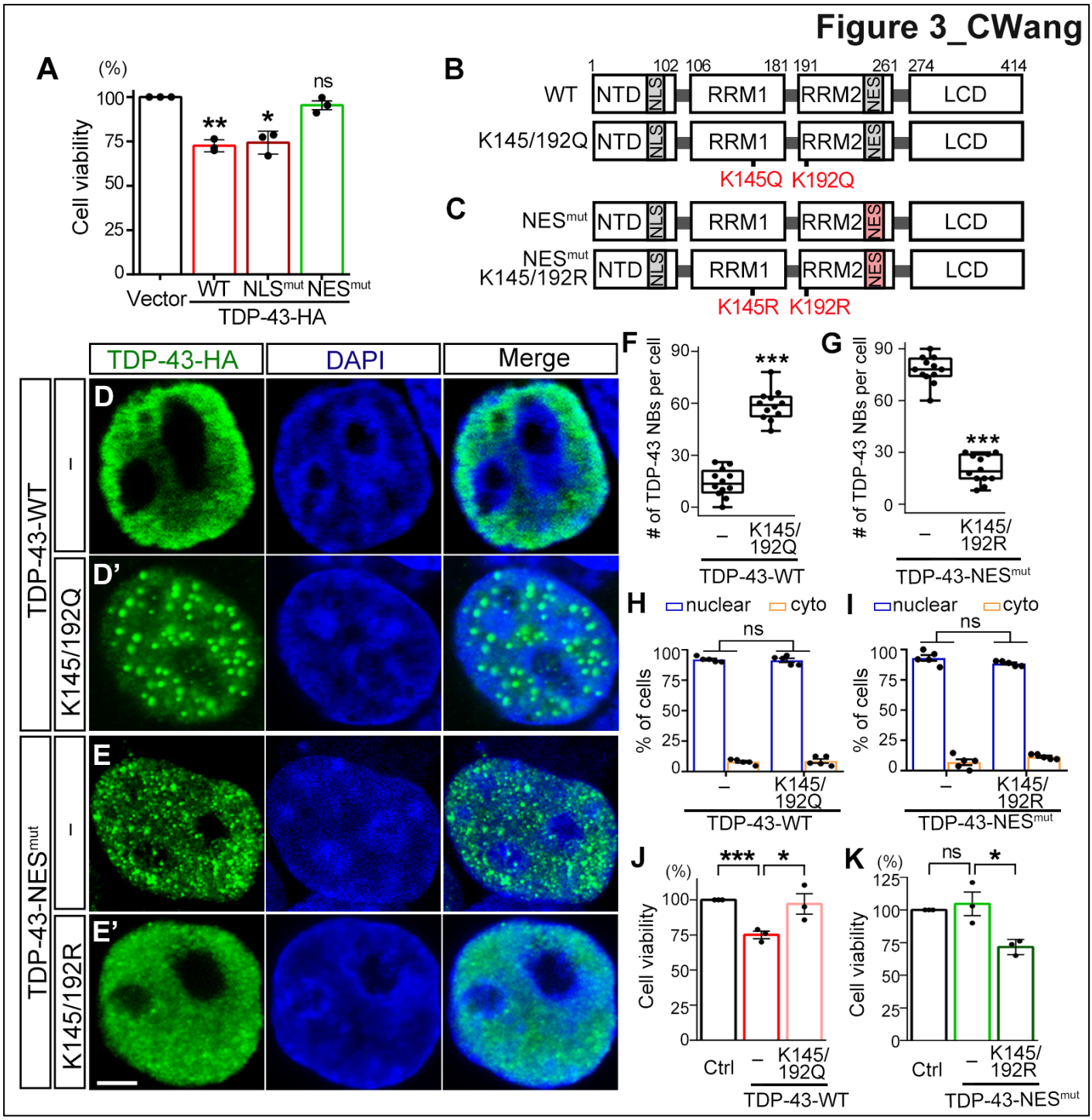

812

Figure 3. Formation of NBs mitigates TDP-43-mediated cytotoxicity.

(**A**) OE of the WT or NLS^{mut} but not NES^{mut} TDP-43 in 293T cells exhibits cytotoxicity and decreases the cell viability, which is measured by the Cell Counting Kit-8 (CCK-8) assay. (**B-C**) Diagrams showing the K145/192Q mutation in the WT TDP-43 and the K145/192R mutation in the NES^{mut} TDP-43, respectively. (**D-E'**) Representative confocal images of the WT (D) and "WT + K145/192Q" TDP-43 (D'), or the NES^{mut} (E) and "NES^{mut} + K145/192R" TDP-43 (E') in 293T cells. (**F-G**) Quantifications of the average numbers of TDP-43 NBs per cell formed in each group in (D-E') as indicated. (**H-I**) Percentages of cells with TDP-43 exclusively in the nucleus (nuclear) or in both the nucleus and the cytoplasm (cyto) in (D-E') are quantified. (**J-K**) The viability of cells expressing the WT or NES^{mut} TDP-43 with the indicated NB-promoting or NB-suppressing mutation is assessed using the CCK-8 assay. Mean ± SEM, except for (F-G) box-and-whisker plots; n = 3 in (A, J-K), n = ~12 cells each group in (F-G), n >100 cells per group in (H-I). $*p < 0.05$, $**p < 0.01$, $***p < 0.001$; ns, not significant; one-way ANOVA in (A), Student's *t*-test in (F-G, J-K), two-way ANOVA in (H-I). Scale bar: 5 μm.

828

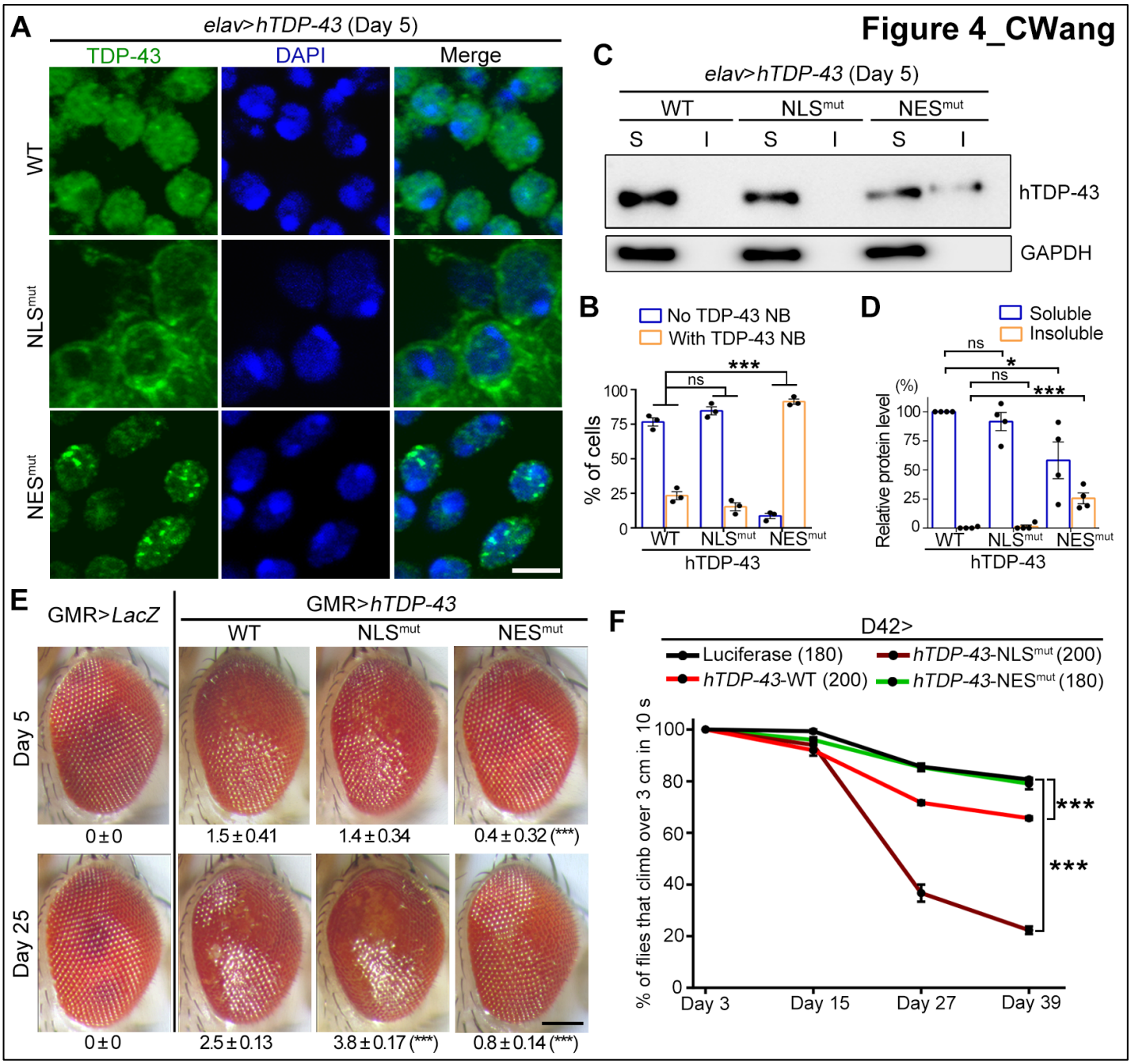

829

Figure 4. Transgenic flies expressing WT, NLS^{mut} or NES^{mut} hTDP-43.

(**A**) Representative confocal images of the fly central brain neurons (*elav*-Gal4) expressing the WT or mutant *hTDP-43* as indicated. The whole-mount fly brains were dissected and immunostained for hTDP-43 (green) and DAPI (blue, to show the nucleus). (**B**) The average percentages of fly neurons with or without TDP-43 NBs are quantified. Mean ± SEM, n = ~100 neurons each group. (**C-D**) Representative image (C) and quantification (D) of Western blot analysis of the WT or mutant hTDP-43 protein extracted from the fly head in RIPA-soluble (S) or RIPA-insoluble (I, resuspended in 9 M of urea) fractions. All protein levels are normalized to GAPDH. The relative level of soluble TDP-43-WT is set to 100%. Mean ± SEM, n = 4. (**E**) Representative z-stack images of the fly eye (GMR-Gal4) expressing the WT or mutant hTDP-43 transgenes as indicated at Day 5 or Day 25. The average degeneration score (mean ± SEM) and the statistic significance (compared to hTDP-43-WT flies) of each group are indicated at the bottom. n = 8 eyes each group. (**F**) The climbing capability of the flies expressing the WT or mutant hTDP-43 in motor neurons (D42-Gal4) is evaluated as percentage of flies climbing over 3 cm in 10 seconds. Control, UAS-*luciferase*. Mean ± SEM, the number of flies tested for each genotype is shown. *p < 0.05, ***p < 0.001; ns, not significant; two-way ANOVA in (B, F), one-way ANOVA in (D-E). Scale bars: 2 μm in (A) and 100 μm in (E).

848

Figure 5_CWang

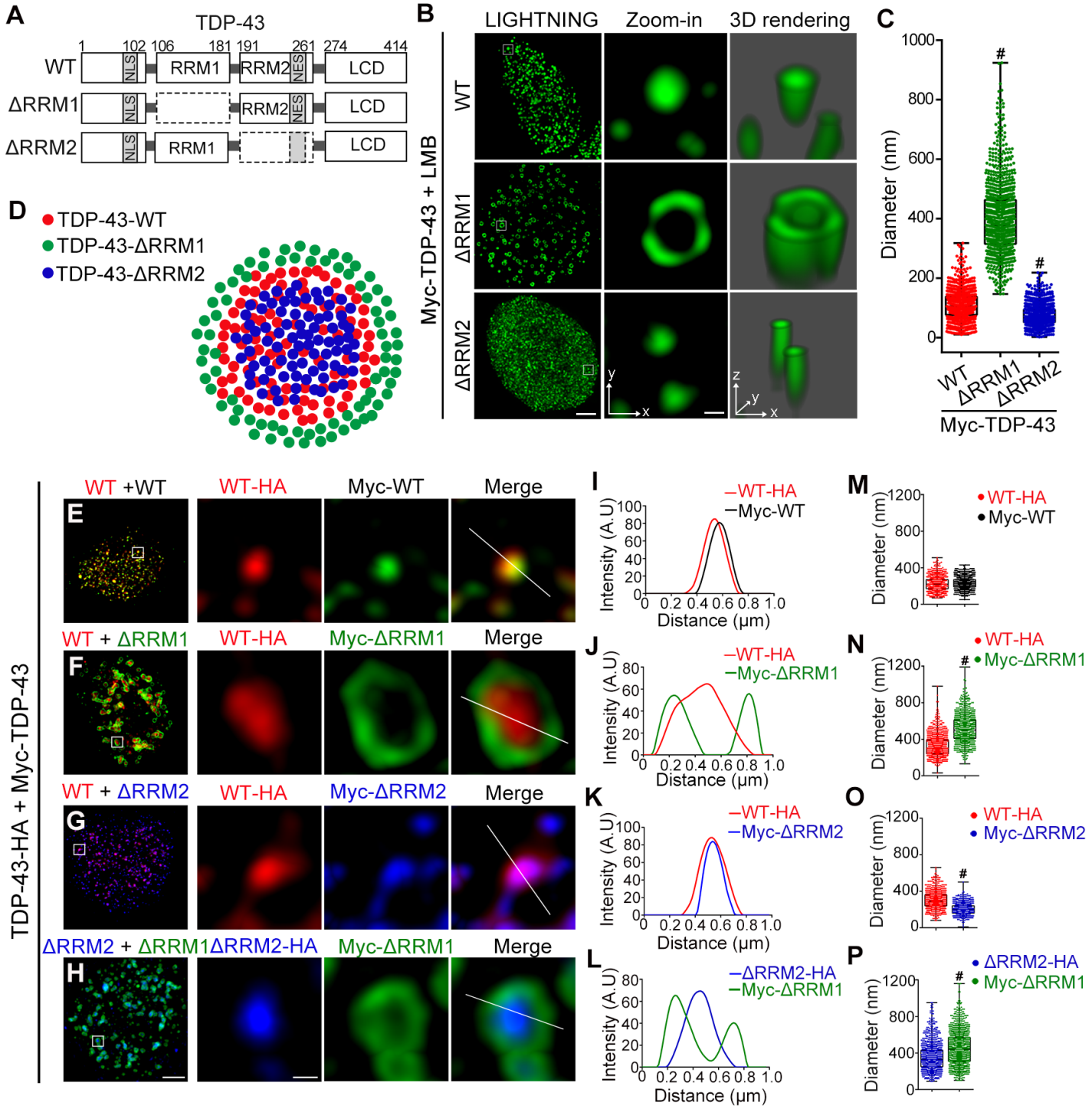

849

Figure 5. The role of RRM1 and RRM2 in maintaining the architecture of TDP-43 NBs.

(**A**) A diagram showing the major functional domains of WT TDP-43 and the ΔRRM1 and ΔRRM2 mutants. (**B**) LIGHTNING super-resolution microscopy of 293T cells transfected with Myc-TDP-43-WT, ΔRRM1 or ΔRRM2 and treated with LMB. Higher magnification images (zoom-ins) and 3D renderings of the boxed areas are shown. (**C**) The average diameters of the WT, ΔRRM1 and ΔRRM2 TDP-43 nuclear structures in (B) are quantified. (**D**) A schematic model of the core-shell architecture of TDP-43 NBs (red) and the distinct distribution of ΔRRM1 (green) and ΔRRM2 (blue). (**E-H**) LIGHTNING multicolor super-resolution microscopy and higher magnification images of representative LMB-induced TDP-43 NBs. Cells are co-transfected with a combination of HA- or Myc-tagged WT, ΔRRM1 or ΔRRM2 TDP-43 as indicated. (**I-P**) The intensity profiles (I-L) along the indicated lines and the average diameters (M-P) of TDP-43 NBs in each group are shown. The box-and-whisker plots with the value of each NB measured are shown. n = ~900 NBs in (C, M-P) for each group from pooled results of at least 3 independent repeats; $^{\#}p < 0.0001$; one-way ANOVA in (C) and Student's *t*-test in (M-P). Scale bars: 5 μm in (B), 2 μm in (E-H) and 200 nm in the zoom-ins.

866

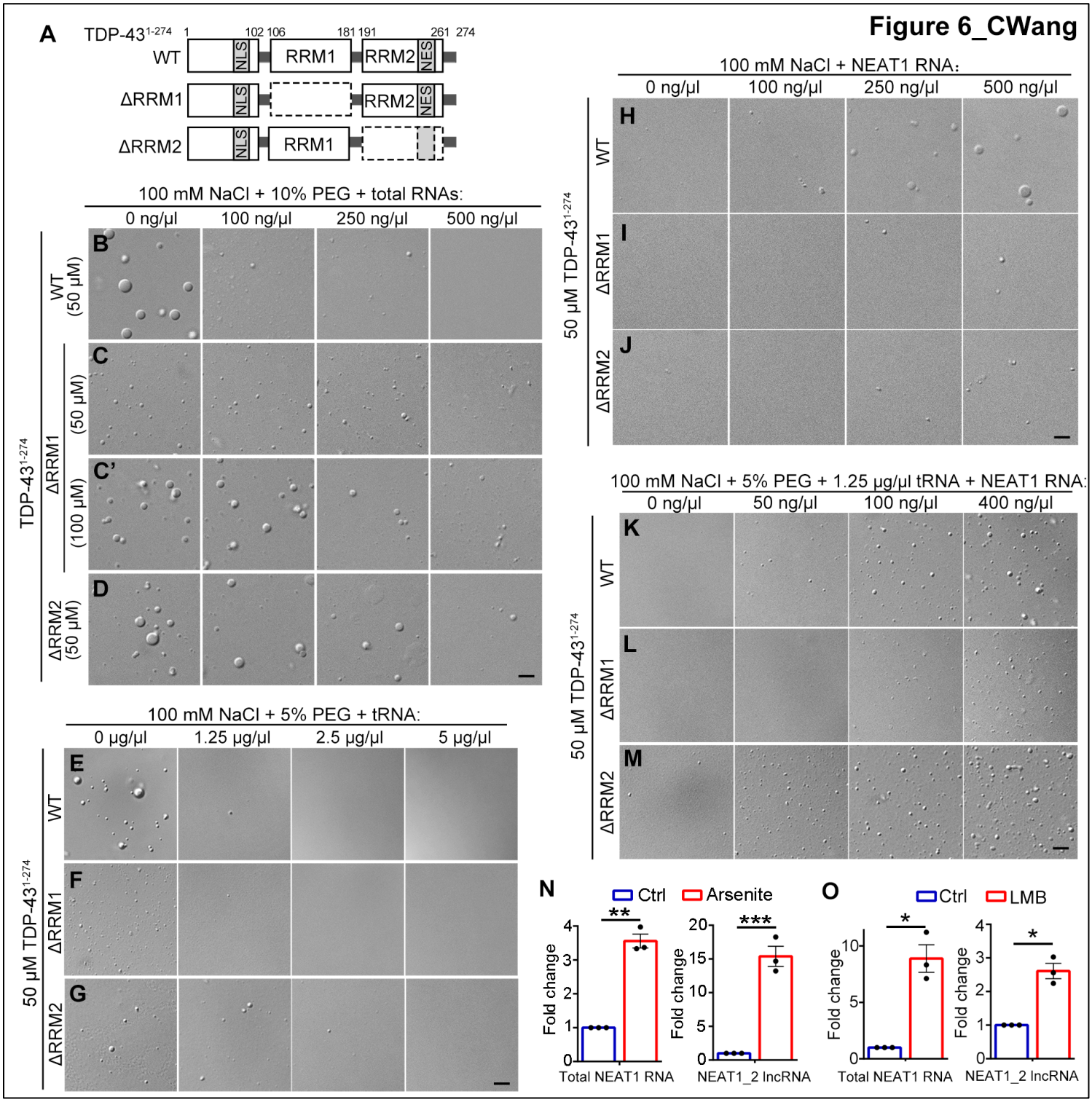

867

868 **Figure 6. The effects of different RNAs on TDP-43 LLPS *in vitro*.**

869 (**A**) A diagram showing the WT, ΔRRM1 and ΔRRM2 of TDP-43$^{1-274}$. (**B-D**) The total RNA
870 extracts, (**E-G**) tRNA, and (**H-J**) lncRNA *NEAT1* are added into the *in vitro* LLPS assay of WT,
871 ΔRRM1 and ΔRRM2 TDP-43$^{1-273}$ as indicated. C', a higher concentration of ΔRRM1 is also
872 included in order to start the suppression assay with large LDs as those of WT TDP-43. (**K-M**)
873 tRNA-mediated suppression of TDP-43 LLPS can be antagonized by increasing *NEAT1* RNA
874 levels. The concentrations of NaCl, the crowding agent PEG, TDP-43 proteins and RNAs used in
875 the *in vitro* assays are as indicated. (**N-O**) Cellular stress induced by arsenite (N) or LMB (O)
876 increases *NEAT1* RNA levels in mouse primary neurons compared to the vehicle control PBS
877 and ethanol, respectively. Mean ± SEM, n = 3; *$p < 0.05$, **$p < 0.01$, ***$p < 0.001$; Student's *t*-test.
878 Scale bars: 2 μm.
879

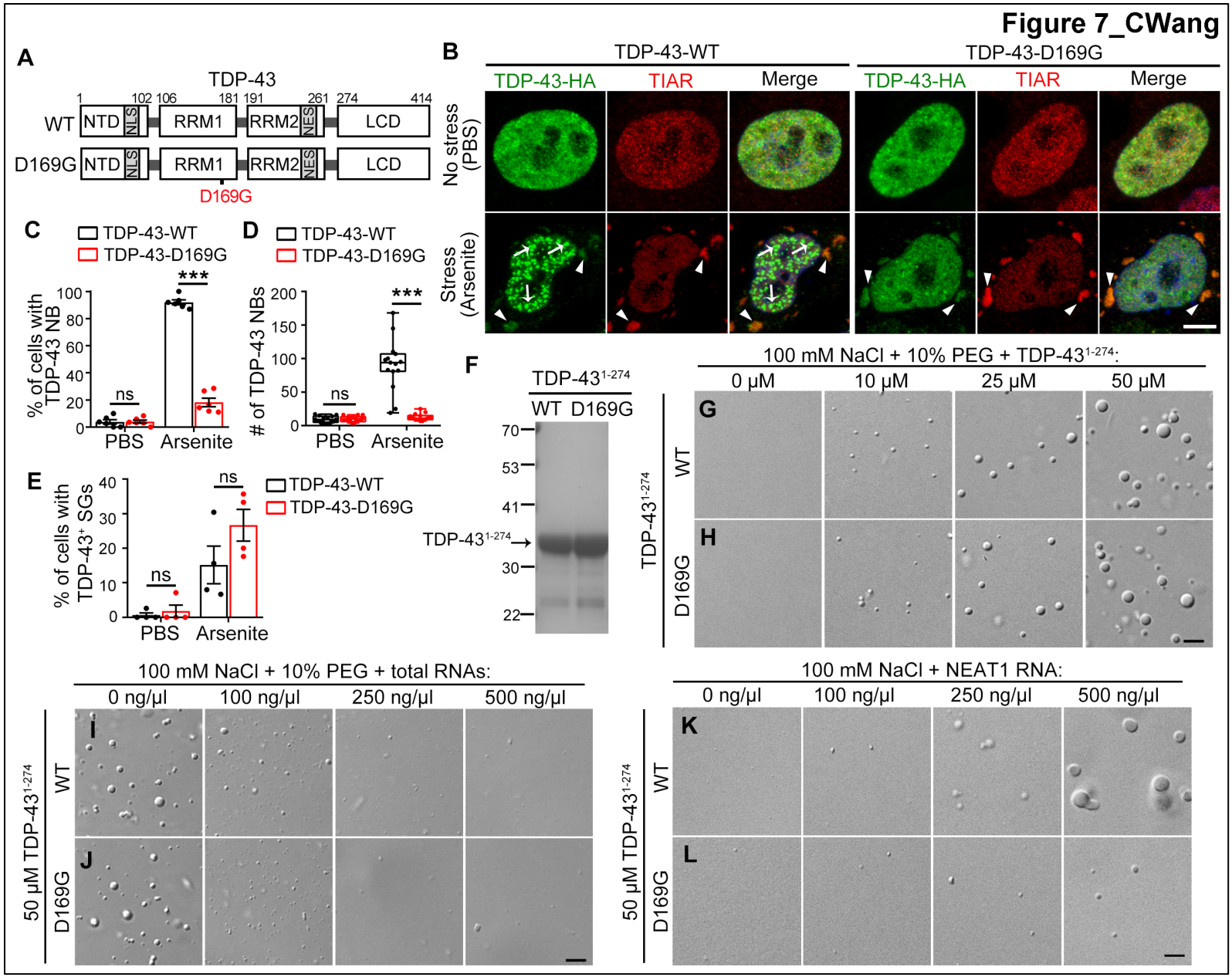
Figure 7_CWang
A
TDP-43
WT
D169G
NTD
NLS
RRM1
RRM2
NES
LCD
D169G
B
TDP-43-WT
TDP-43-D169G
TDP-43-HA
TIAR
Merge
No stress (PBS)
Stress (Arsenite)
C
TDP-43-WT
TDP-43-D169G
% of cells with TDP-43 NB
ns
***
PBS
Arsenite
D
# of TDP-43 NBs
E
% of cells with TDP-43+ SGs
F
TDP-43 1-274
WT D169G
TDP-43 1-274
G
H
100 mM NaCl + 10% PEG + TDP-43 1-274:
0 μM
10 μM
25 μM
50 μM
I
J
100 mM NaCl + 10% PEG + total RNAs:
0 ng/μl
100 ng/μl
250 ng/μl
500 ng/μl
50 μM TDP-43 1-274
K
L
100 mM NaCl + NEAT1 RNA:

880

Figure 7. The ALS-associated D169G mutation impairs the ability of TDP-43 to form stress-induced NBs and *NEAT1*-promoted LDs.

(**A**) A diagram showing WT and D169G mutant TDP-43. (**B**) Representative confocal images of HeLa cells transfected with WT or D169G TDP-43 in the absence (PBS) or presence of arsenite. Green, TDP-43-HA (anti-HA); Red, anti-TIAR for SGs; Blue, DAPI staining for DNA (nucleus). Arrows, TDP-43 NBs; arrowheads, TDP-43^{+} SGs. (**C-E**) The percentage of cells with TDP-43 NBs (C), the average count of TDP-43 NBs per cell (D) and the percentage of cells with TDP-43^{+} SGs (E) in (B) are quantified. Mean ± SEM, except for (D) box-and-whisker plots; n = ~100 cells for each group in (C, E) and n = ~15 cells for each group in (D) from pooled results of 3 independent repeats; ***p < 0.001; ns, not significant; Student's *t*-test. (**F**) Coomassie blue staining confirming the purified WT and D169G TDP-43$^{1\text{-}274}$ proteins used in the *in vitro* LLPS assays. (**G-H**) Both WT and D169G TDP-43 form LDs by LLPS in a dose-dependent manner. (**I-J**) Suppression of the *in vitro* LLPS of WT and D169G TDP-43 by total RNA extracts. (**K-L**) Promotion of TDP-43 LLPS by *NEAT1* RNA is dramatically reduced in the D169G TDP-43. The concentrations of NaCl, TDP-43, PEG and RNA used in the *in vitro* assays are as indicated. Scale bars: 5 μm in (B) and 2 μm in (G-L).

Supplementary Information for

Stress induces cytoprotective TDP-43 nuclear bodies through lncRNA *NEAT1*-promoted phase separation

Chen Wang, Yongjia Duan, Gang Duan, Zhiwei Ma, Kai Zhang, Xue Deng, Beituo Qian, Jinge Gu, Shuang Zhang, Lin Guo, Cong Liu, and Yanshan Fang

Correspondence to: fangys@sioc.ac.cn

This PDF file includes:

Online Methods

Figure S1 to S7

Captions for Movies S1 to S2

Other Supplementary Data for this manuscript include the following:

Movies S1 to S2

Online Methods

Plasmids and constructs

The pcDNA3.1-TDP-43-HA and pCMV-myc-TDP-43 plasmids were as previously described (*99*) and used as the templates to generate the following plasmids. The pcDNA3.1-TDP-43-NES^{mut}, NLS^{mut}, D169G and M337V-HA plasmids were generated by site-directed mutagenesis using the Fast Mutagenesis Kit II (Vazyme). The pcDNA3.1-TDP-43-K145/192Q-HA and pcDNA3.1-TDP-43-NES^{mut}-K145/192R-HA plasmids were generated by site-directed mutagenesis using the Fast Mutagenesis Kit MultiS (Vazyme). The pCMV-myc-TDP-43$^{1-274}$ pCMV-myc-TDP-43-ΔRRM1, and pCMV-myc-TDP-43-ΔRRM2 plasmids were generated by PCR using the pCMV-myc-TDP-43 plasmid as a template. To generate the pCAG-GFP-TDP-43 plasmid, the GFP coding sequence was amplified from pcDNA3.1-GFP-AXR3 (a gift from Dr. Z. Zhang) by PCR and then subcloned into a pCAG-hTDP-43 plasmid (*99*) using the ClonExpress MultiS One Step Cloning Kit (Vazyme).

For lentivirus infection of mouse primary neurons, the pLenti-hSyn-TDP-43-HA plasmid was generated by PCR using the pcDNA3.1-TDP-43-HA as a template and sub-cloned into the pLenti-hSyn vector (a gift from Dr. Y. Chen).

For generation of transgenic fly lines, the WT and mutant UAS-hTDP-43 constructs were generated by PCR using the above plasmids as a template and sub-cloned into the pBID-UASC-6*Myc vector (100) between the KpnI and ApaI sites.

For *Escherichia coli* (*E. coli*) expression, the pET28a-6×His-sumo-TDP-43, sumo-TDP-43-$^{1-274}$, His-TDP-43$^{1-274}$, His-TDP-43$^{1-274}$-ΔRRM1, His-TDP-43$^{1-274}$-ΔRRM2 and His-TDP-43$^{1-274}$-D169G constructs were generated by PCR using the above WT or mutant TDP-43 plasmid as a template and were sub-cloned into a pET28a-6×His (a gift from Dr. L. Pan) or pET28a-6×His-sumo (a gift from Dr. J. Zhou) vector.

For *in vitro* transcription of NEAT1 RNA, the pcDNA3.1-NEAT1 was generated by PCR using the pEGFP-C1-mNEAT1 plasmid (a gift from Dr. L. Chen) as a template and sub-cloned into the pcDNA3.1 vector.

The primers used for PCR to generate the expression plasmids are summarized below. All constructs were verified by sequencing to ensure the integrity of the cloned open reading frames.

pcDNA3.1-TDP-43-HA:

5'- CGTTTAAACGGGCCCTCTAGAGCCACCATGTCTGAATATATTCGG -3'

5'-CACAGTGGCGGCCGCCTAAGCGTAGTCTGGGACGTCGTATGGGTACATTCCCCAG CCAGAAG -3'

pcDNA3.1-TDP-43-NLS^{mut}-HA:

5'- TAACGCAGCAGCAATGGATGAGACAGATGCTTCATCA -3

5'- CCATTGCTGCTGCGTTATCTTTTGGATAGTTGACAACATACA -3

pcDNA3.1-TDP-43-NES^{mut}-HA:

5'- GGCAGCGCAGTCTGCATGTGGAGAGGACTTGATCATTAAAGG -3

5'- ATGCAGACTGCGCTGCCTGATCATCTGCAAATGTAACAAAGG -3

pLenti-hSyn-TDP-43-HA:

5'- AGAGCGCAGTCGAGAGGATCCGCCACCATGTCTGAATATATTCGG -3'

5'- GATAAGCTTGATATCGAATTCTCATTAAGCGTAGTCTGGGACGTCG -3'

pBID-UASC-TDP-43-Myc:

5'- CGGCCGCGGCTCGAGGGTACCATGTCTGAATATATTCGGGTAACCG -3'

5'- GAGTTTTTGTTCGAAGGGCCCTCTAGACTCGAGCATTCCCCAGCCAGAAGACTT-3'

pBID-UASC-TDP-43-NLS^{mut}-Myc:

5'- CGGCCGCGGCTCGAGGGTACCATGTCTGAATATATTCGGGTAACCG -3'

5'- GAGTTTTTGTTCGAAGGGCCCTCTAGACTCGAGCATTCCCCAGCCAGAAGACTT-3'

pBID-UASC-TDP-43-NES^{mut}-Myc:

5'- CGGCCGCGGCTCGAGGGTACCATGTCTGAATATATTCGGGTAACCG -3'

5'- GAGTTTTTGTTCGAAGGGCCCTCTAGACTCGAGCATTCCCCAGCCAGAAGACTT-3'

pcDNA3.1-TDP-43-K145/192Q-HA:

5'- TCATTCACAGGGGTTTGGCTTTGTTCGTTTT -3

5'- CAAACCCCTGTGAATGACCAGTCTTAAGATCTTTCTTG -3

5'- GCAGACAAGTGTTTGTGGGGCGCTGTAC -3

5'- CACAAACACTTGTCTGCTTCTCAAAGGCTCATCTT -3

pcDNA3.1-TDP-43-NES^{mut}-K145/192R-HA:

5'- TCATTCAAGGGGGTTTGGCTTTGTTCGTTTT -3

5'- CAAACCCCCTTGAATGACCAGTCTTAAGATCTTTCTTG -3

5'- GCAGAAGAGTGTTTGTGGGGCGCTGTAC -3

5'- CACAAACACTCTTCTGCTTCTCAAAGGCTCATCTT -3

pcDNA3.1-TDP-43-D169G-HA:

5'- ATGATAGGTGGACGATGGTGTGACTGCAAACT -3'

5'- CATCGTCCACCTATCATATGTCGCTGTGACATTACTTTC -3'

pcDNA3.1-TDP-43-M337V-HA:

5'- GGTATGGTGGGCATGTTAGCCAGCCAGCAGAA -3'

5'- AACATGCCCACCATACCCCAACTGCTCTGTAGTGC -3'

pCMV-Myc-TDP-43:

5'- ATGGCCATGGAGGCCCGAATTCATGTCTGAATATATT-3'

5'- CCGCGGCCGCGGTACCTCGAGCTACATTCCCCAGCCAGAAGAC -3'

pCMV-Myc-TDP-43$^{1–274}$:

5'- ATGGCCATGGAGGCCCGAATTCATGTCTGAATATATT -3'

5'- CCGCGGCCGCGGTACCTCGAGCTATCCACTTCTTTCTAACTGTCTATTGC -3'

pCMV-Myc-TDP-43-ΔRRM1:

5'- ATGGCCATGGAGGCCCGAATTCATGTCTGAATATATT -3'

5'- CCGCGGCCGCGGTACCTCGAGCTACATTCCCCAGCCAGAAGAC -3'

pCMV-Myc-TDP-43-ΔRRM2:

5'- ATGGCCATGGAGGCCCGAATTCATGTCTGAATATATT -3'

5'- CCGCGGCCGCGGTACCTCGAGCTACATTCCCCAGCCAGAAGAC -3'

pCAG-GFP-TDP-43:

5'- CATCATTTTGGCAAAGAATTCCACCATGGTGAGCAAGGGCGAGG -3'

5'- CAGACATGCTTCCGCCCTTGTACAGCTCGTCCATGCC -3'

5'- CGAGCTGTACAAGGGCGGAAGCATGTCTGAATATATTCGGGTAACCG -3'

5'- GCTCCCCGGGGGTACCTCGAGCTATTACATTCCCCAGCCAGAAGACTT -3'

pET28a-6×His-TDP-43$^{1-274}$:

5'- CAGCAAATGGGTCGCGGATCCATGTCTGAATATATTCGGGTAACCG -3'

5'- GTGGTGGTGGTGGTGCTCGAGTTAACTTCTTTCTAACTGTCTATTGCTATTG -3'

pET28a-6×His-TDP-43$^{1-274}$-ΔRRM1:

5'- CAGCAAATGGGTCGCGGATCCATGTCTGAATATATTCGGGTAACCG -3'

5'- GTGGTGGTGGTGGTGCTCGAGTTAACTTCTTTCTAACTGTCTATTGCTATTG -3'

pET28a-6×His-TDP-43$^{1-274}$-ΔRRM2:

5'- CAGCAAATGGGTCGCGGATCCATGTCTGAATATATTCGGGTAACCG -3'

5'- GTGGTGGTGGTGGTGCTCGAGTTAACTTCTTTCTAACTGTCTATTGCTATTG -3'

pET28a-6×His-TDP-43$^{1-274}$-D169G:

5'- CAGCAAATGGGTCGCGGATCCATGTCTGAATATATTCGGGTAACCG -3'

5'- GTGGTGGTGGTGGTGCTCGAGTTAACTTCTTTCTAACTGTCTATTGCTATTG -3'

pET28a-6×His-sumo-TDP-43:

5'- AGAGAACAGATTGGTGGATCCATGTCTGAATATATTCGGGTAACCG -3'

5'-TTGTCGACGGAGCTCGAATTCTTACATTCCCCAGCCAGAAGAC -3'

pET28a-6×His-sumo-TDP-43-$^{1-274}$:

5'- AGAGAACAGATTGGTGGATCCATGTCTGAATATATTCGGGTAACCG -3'

5'- TTGTCGACGGAGCTCGAATTCTTATCCACTTCTTTCTAACTGTCTATTGC -3'

pcDNA3.1-NEAT1:

5'- CGTTTAAACGGGCCCTCTAGAGAGTTAGTGACAAGGAGGGCTCG -3'

5'- ATATCCAGCACAGTGGCGGCCGCTTCAATCTCAAACCTTTATTTTGCTG-3'

Cell cultures and transfection

293T and HeLa cells were cultured in Dulbecco's Modified Eagle Medium (Sigma, D0819)

supplemented with 10% (v/v) fetal bovine serum (FBS, BioWest) and 1% penicillin/streptomycin at 37˚C in 5% CO_2. Transient transfection was performed using Lipofectamine™ 3000 (Invitrogen) in Opti-MEM (Invitrogen). Cells were transfected for at least 24h before the subsequent drug treatments or examinations.

Pharmacological experiments:

Arsenite treatment: HeLa or 293T cells were grown on coverslips in a 24-well plate and transfected with the indicated plasmids for 24 h. Cells were then treated with 250 μM of $NaAsO_2$ or PBS for 30 min, prior to fixation with 4% paraformaldehyde. For the recovery experiments, the culture medium containing $NaAsO_2$ was removed and the cells were incubated in fresh medium for indicated time prior to fixation.

LMB treatment: For the nuclear export inhibition assays, LMB was added into the culture medium after 6h transfection at indicated final concentrations.

CHX treatment: For the pulse-chase assays, CHX was added into the medium at each time point at a final concentration of 25 ng/ml.

MG132 treatment: For the proteasomal inhibition assays, MG132 was added into the medium at each time at a final concentration of 25 μM.

CQ treatment: For autophagy inhibition assays, CQ was added into the medium at each time at a final concentration of 25 mM.

The cells incubated in the culture medium with the above drugs for indicated time before fixation for immunocytochemistry or western blotting analysis.

Immunocytochemistry and immunohistochemistry assays

HeLa or 293T cells grown on coverslips pre-coated with PLL (Sigma) in a 24-well plate were transfected and treated as described above. The cells were then fixed in 4% paraformaldehyde in PBS for 15 min at room temperature (RT), permeabilized in 0.5% Triton X-100 (Sigma) in PBS for 15 min and blocked with 3% goat serum in PBST (0.1% Triton X-100 in PBS) for 1h at RT.

For immunostaining of the whole-mount *Drosophila* brain, fly brains were dissected on ice and immediately fixed in 4% paraformaldehyde in PBS for 30 min at RT and permeabilized with 0.5% Triton X-100 in PBS overnight at 4°C overnight.

The above primary and secondary antibodies were then incubated in the blocking buffer at 4°C overnight or at RT for 1-2 h. After 3 washes with PBST, cells were mounted on glass slides using the VECTASHIELD Antifade Mounting Medium with DAPI (Vector Laboratories).

Confocal and super-resolution imaging

Fluorescent confocal images were taken with Leica TCS SP8 confocal microscopy system using a 63X or 100X oil objective (NA=1.4). Super-resolution images were captured using the Leica SP8 LIGHTNING confocal microscope, which allowed simultaneous multicolor imaging in super-resolution down to 120 nm. Confocal or super-resolution images were then processed in LAS X (Leica) and assembled into figures using Adobe Photoshop CS6.

Live cell imaging

HeLa cells transfected with pCAG-GFP-TDP-43 were grown on Nunc™ Lab-Tek™ Chambered Coverglass (Thermo) for 24 h before the cells were treated with 250 μM of $NaAsO_2$. For live cell imaging, the chambered coverglasses were placed in the Incubation System for Microscopes (Tokai Hit) and maintained at 37˚C in 5% CO_2 for the duration of the experiment. Time-lapse images were captured using the Leica TCS SP8 confocal microscopy system every 10 min for about 1 h.

Fluorescence recovery after photobleaching (FRAP) assay

The PFRP assay was performed using the FRAP module of the Leica SP8 confocal microscopy system. In brief, each GFP-TDP-43 NB was bleached using a 488 nm laser at 100% laser power for approximately 5 s. After photobleaching, time-lapse images were captured every 10 s for the about 5 min. For each indicated time point (t), the fluorescence intensity within the bleached NB

was normalized to the fluorescence intensity of a nearby, unbleached NB (to control for photobleaching during prolonged live imaging). The normalized fluorescence intensity of pre-bleaching was set to 100% and the normalized fluorescence intensity at each time point (I_t) was used to calculate the fluorescence recovery according to the following formula: FR(t) = $I_t/I_{pre\text{-}bleaching}$. Image J was used for quantification and GraphPad Prism to plot and analyze the FRAP experiments.

Antibodies

The following antibodies were used for Western blotting, immunoprecipitation and immunofluorescence assays: mouse anti-FLAG (Sigma, F3165), mouse anti-HA (Proteintech, 66006-1), rabbit anti-c-Myc (Sigma, c3956), rabbit anti-TDP-43 (Proteintech, 10782-2-AP), anti-β-Tubulin III (Sigma, T2200), rabbit anti-TIAR (Cell Signaling Technology, 8509S), rabbit anti-SC35 (Abcam, ab204916), rabbit anti-SFPQ (Abcam, ab177149), rabbit anti-TAF9 (Abcam, ab169784), rabbit anti-PML (Abcam, ab179466), and chicken anti-MAP2 (Abcam, ab5392). HRP conjugated secondary antibodies: goat anti-mouse (Sigma, A4416) and goat anti-rabbit (Sigma, A9169). Fluorescent secondary antibodies: goat anti-mouse-Alexa Fluor 488 (Life Technologies, A11029), goat anti-rabbit-Alexa Fluor 568 (Life Technologies, A11036) and goat anti-Chicken-Alexa Fluor 568 (Life Technologies, A11041).

Protein extraction and Western blotting

Total protein was extracted from cells in a 2% SDS extraction buffer (50 mM Tris pH 6.8, 2% SDS, 1% mercaptoethanol, 12.5% glycerol and 0.04% bromophenol blue) containing the protease inhibitor cocktail (Roche, 04693132001). For separation of soluble and insoluble proteins, cells or fly heads were lysed on ice in a RIPA buffer (50 mM Tris pH 8.0, 150 mM NaCl, 1% NP-40, 5 mM EDTA, 0.5% sodium deoxycholate, 0.1% SDS) supplemented with protease and phosphatase inhibitors (Roche). After sonication, the homogenates were centrifuged at 16,000 g for 15min at 4°C. The supernatant was used as the soluble fraction and the pellets

209 containing the insoluble fraction were dissolved in a urea buffer (9 M urea, 50 mM Tris buffer, pH
210 8.0) after wash.

211 All protein samples were then boiled at 100°C for 5 min and separated using a 10% Bis-Tris
212 SDS-PAGE (Invitrogen). Detection was performed using the High-sig ECL Western Blotting
213 Substrate (Tanon). Images were captured using an Amersham Imager 600 (GE Healthcare) and
214 densitometry was measured using ImageQuant TL Software (GE Healthcare). The contrast and
215 brightness were optimized equally using Adobe Photoshop CS6. All experiments were
216 normalized to tubulin or GAPDH as indicated in the figures.

217

218 **Cell viability assay**

219 Transfected 293T cells were seeded in 96-well plates (Corning) at the density of 9×10^3 cells/well
220 and cultured in 100 μL of culture medium. Otherwise, cell viability was examined 48-72 h after
221 transfection using the Cell Counting Kit-8 (CCK-8) (Dojindo), according to the manufacturer's
222 instructions. Briefly, 10 μL of the CCK-8 solution were added to each well and incubated at 37°C
223 for 2.5 h. Finally, the absorbance at 450 nm was measured with a Synergy2 microplate reader
224 (BioTek Instruments).

225

226 **Mouse care and surgical procedures**

227 All mouse procedures were performed in compliance with the institutional guidelines on the
228 scientific use of living animals at Interdisciplinary Research Center on Biology and Chemistry,
229 the Chinese Academy of Sciences (CAS). "Principles of laboratory animal care" (NIH publication
230 No. 86-23, revised 1985) were followed. Animal distress and conditions requiring euthanasia
231 were addressed and the number of animals used was minimized.

232

233 **Lentivirus production and primary neuron culture**

234 To generate lentivirus for infecting primary neurons, 293T cells were co-transfected with
235 pLenti-hSyn-TDP-43-HA, psPAX2 and pMD2.G with a ratio of 4:2:1 in Opti-MEM medium using

Lipofectamine™ 2000. Culture supernatant was collected at 48 h after transfection and passed through a 0.45-μm filter. Viral particles were concentrated from culture supernatants by Lenti-X™ Concentrator (Clontech). Viral pellets used for neuronal infection were resuspended in Neurobasal medium (Invitrogen).

Primary cortical neuron were isolated from C57BL/6 mouse cortex at embryonic day 17 (E17) and cultured in serum-free Neurobasal medium (Invitrogen) supplemented with 2% B27, GlutaMax, and penicillin-streptomycin (Invitrogen). At 7 days in vitro (DIV), neurons were infected with pLenti-hSyn-TDP-43-HA for 5 days before extraction for RNA or immunofluorescence.

RNA extraction and real-time quantitative PCR

For quantitative PCR (qPCR), total RNA was isolated from mouse primary neuron using TRIzol (Invitrogen) according to the manufacturer's instruction. After DNase (Promega) treatment, the reverse transcription reactions were performed using All-in-One cDNA Synthesis SuperMix kit (Bimake). The cDNA was then used for real-time qPCR using the SYBR Green qPCR Master Mix (Bimake) with the QuantStudio™ 6 Flex Real-Time PCR system (Life Technologies). The mRNA levels of GAPDH were used as an internal control to normalize the mRNA levels of NEAT1. The qPCR primers used in this study are listed below:

Total mNEAT1:

5'- ACTCTTGCCCCTCACTCTGA -3'

5'- CAGGGTGTCCTCCACCTTTA -3';

mNEAT1_2:

5'- CCCACACCTCAGTGGTTTCT -3'

5'- ACAGAACCAAGGCACAATCC -3';

mGAPDH:

5'- CACCATCTTCCAGGAGCGAG -3'

5'- CCTTCTCCATGGTGGTGAAGAC -3';

263

264 **Purification of TDP-43 proteins**

265 WT or mutant TDP-43 protein was expressed in BL21 (DE3) *E. coli* (TransGenBiotech,
266 CD601-03) at 19°C for 16 h after induction by adding 100 μM of IPTG as previously described
267 (*46*). In brief, cells were harvested by centrifugation at 4000 rpm for 20 min at 4 °C and lysed in
268 50 mL of lysis buffer (50 mM Tris-HCl, 500 mM NaCl, pH 8.0, 10 mM imidazole, 4 mM
269 β-mercaptoethanol, 1 mM PMSF, and 0.1 mg/mL RNase A). After cell lysates were filtered with a
270 0.22 μm filter, the protein was purified using Ni columns (GE Healthcare, USA) and then eluted in
271 an elution buffer (50 mM Tris-HCl, 500 mM NaCl, pH 8.0, 250 mM imidazole and 4 mM
272 β-mercaptoethanol). The proteins were further purified using the Superdex 200 16/600 columns
273 (GE Healthcare) in a buffer containing 50 mM Tris-HCl pH 7.5, 300 mM NaCl and 2 mM DTT,
274 and freshly frozen in liquid nitrogen and stored at -80 °C. RNase A was routinely added in cell
275 lysates and administrated again before chromatography during the protein purification procedure.
276 All purified proteins were confirmed by Coomassie brilliant blue staining and Western blotting
277 before use.

278

279 **RNA-binding dot-blot assay**

280 Purified WT or mutant TDP-43 protein was diluted in a blotting buffer (50 mM Tris-HCl, pH 7.5,
281 300 mM NaCl, and 5% glycerol) and blotted onto a 0.45 μm nitrocellulose membrane. The
282 membranes were left to dry at room temperature for 30 min and then stained with Ponceau S for
283 10s. Images were captured using an Amersham Imager 600 (GE Healthcare). After the images
284 were captured using an Amersham Imager 600 (GE Healthcare), the membranes were washed
285 with PBST (0.05% TWEEN 20 in PBS) for 30 min and then incubated in the PBST containing 25
286 ng/μl total RNAs or NEAT1 RNA for 1h with gentle rocking and rotation at room temperature. The
287 membranes were then washed in PBST and incubated in the SYBR™ Gold Nucleic Acid Gel
288 Stain (Invitrogen) for 10 min. RNAs bound to the membranes were imaged and examined using
289 the Gel Image System (Tanon).

290

291 ***In vitro* phase separation and RNA buffering assay**

292 For the *in vitro* LLPS experiments, purified WT or mutant TDP-43 protein was mixed with NaCl at
293 indicated concentrations in a phase separation buffer (50 mM Tris-HCl, pH 7.5 and 5-10% (w/v)
294 PEG 8000 (Sigma)) and incubated for 1 min at room temperature. For the RNA buffering assay,
295 the TDP-43 proteins were incubated with total RNAs, tRNA or NEAT1 RNA in the above phase
296 separation buffer with NaCl at indicated concentrations as shown in the figures. Finally, 5 μL of
297 each sample was pipetted onto a coverslip and imaged using a Leica microscope with differential
298 interference contrast (DIC). The total RNAs were extracted from HeLa cells using TRIzol
299 (Invitrogen) according to the manufacturer's instructions. Yeast tRNA was purchased from
300 Invitrogen. The NEAT1 RNA was *in vitro* transcribed and purified using HiScribe™ T7 Quick High
301 Yield RNA Synthesis Kit (NEB). Total RNAs and NEAT1 RNA were used within one day of
302 production.

303

304 ***Drosophila* strains**

305 Flies tested in this study were raised on standard cornmeal media and maintained at 25 °C and
306 60% relative humidity. The following strains were obtained from the Bloomington *Drosophila*
307 Stock Center (BDSC): *D42*-Gal4 (#8816), *elav*-Gal4 (#8760) and UAS-*LacZ* (#8529). The
308 transgenic fly strains of WT and mutant UAS-hTDP-43 were generated by ΦC31
309 integrase-mediated, site-specific integration, which allowed uniform transgene expression across
310 different lines. The attP2 landing site stock used for the fly embryo injection and transformation in
311 this study was y[1] M{vas-int.Dm}ZH-2A w[*]; P{CaryP}attP40 (25C6), and the transgenic
312 pBID-UASC-Luciferase (UAS-Luc) fly strain that was generated using the same approach at the
313 same landing site (*100*) was used as a control.

314

315 **Fly climbing assay**

316 For the climbing assay, ~20 flies per vial, ~10 vials per group were tested. All flies were

317 transferred into an empty polystyrene vial and allowed 10 min for flies to recover. The flies were
318 then gently tapped down to the bottom of the vial and the number of flies that climbed over 3cm
319 within 10 seconds was recorded. The test was repeated three times for each via.
320
321 **Statistical Analysis**
322 Statistical significance in this study is determined by one-way analysis of variance (ANOVA) with
323 Tukey's HSD post-hoc test, two-way ANOVA with Bonferroni's post-hoc test, or unpaired,
324 two-tailed Student's *t*-test with unequal variance at *p < 0.05, **p < 0.01, and ***p < 0.001 as
325 indicated in each figure legend. Error bars represent the standard error of the mean (SEM).

326 **Supplementary Figures**

327

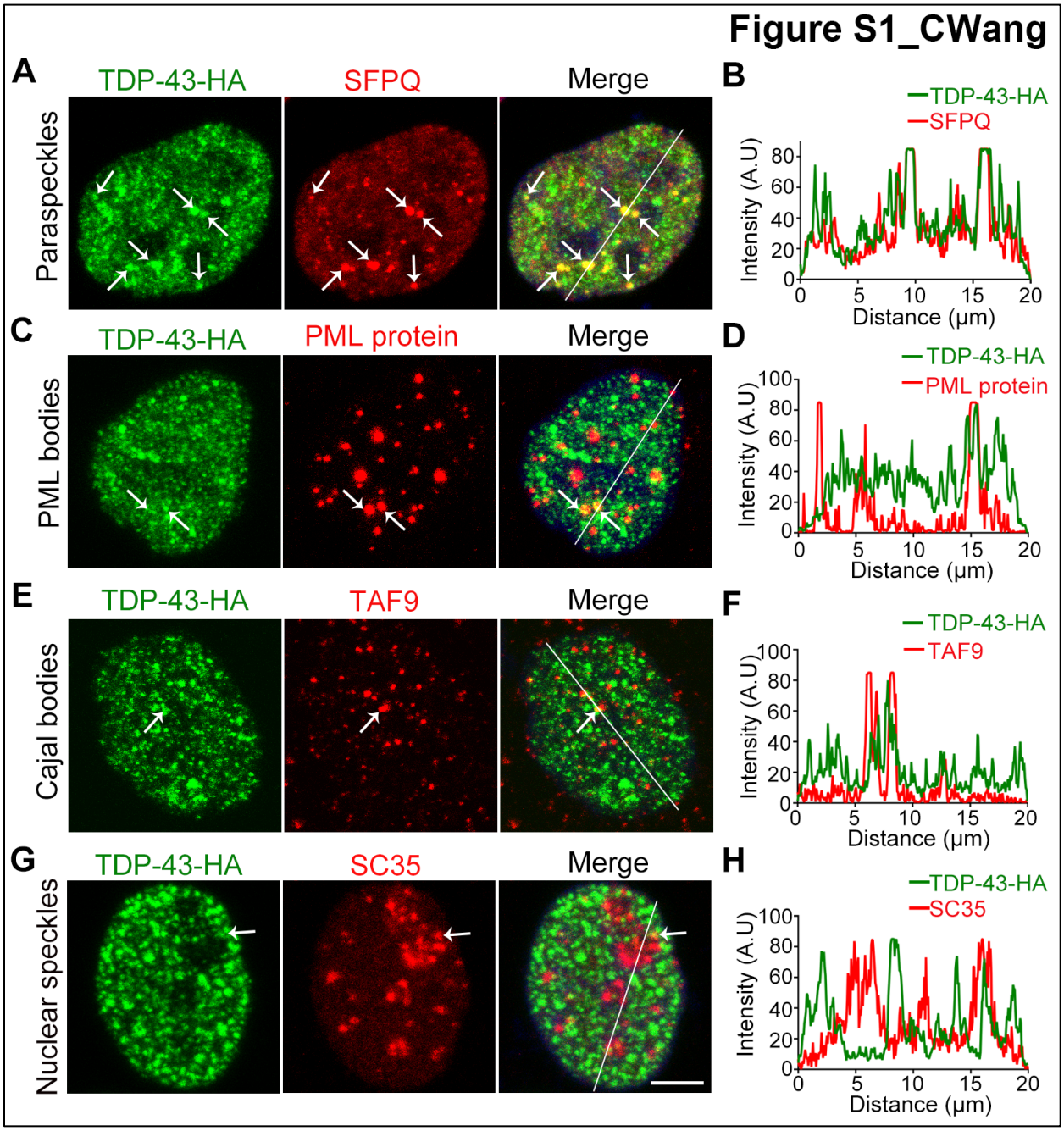

328

Figure S1. Co-immunostaining of TDP-43 with several known NB markers

Representative confocal images of the nucleus of 293T cells transfected with TDP-43-HA and treated with 250 μM $NaAsO_2$ for 30 min. All cells are examined by immunocytochemistry with anti-HA for TDP-43-HA (green) and the indicated antibodies (red): (**A-B**) SFPQ (splicing factor proline-glutamine rich), for paraspeckles (*74*). (**C-D**) PML (promyelocytic leukaemia) protein, for PML bodies (*101*). (**E-F**) TAF9 (TATA-box binding protein associated factor 9) for Cajal bodies (*102*). (**G-H**) SC35 (serine/arginine-rich splicing factor-like protein), for nuclear speckles (*103*). Merged images with DAPI staining (for DNA) are shown. Arrows indicate the examples of co-localization of TDP-43 with the indicated NB markers. The co-localization of TDP-43 with each type of NBs is further evaluated by the line scanning analysis shown in (B), (D), (F) and (H), Scale bar: 5 μm. The results indicate that TDP-43 NBs are well colocalized with paraspeckles, and in a few rare cases partial colocalization with PML bodies, Cajal bodies or nuclear speckles are also spotted.

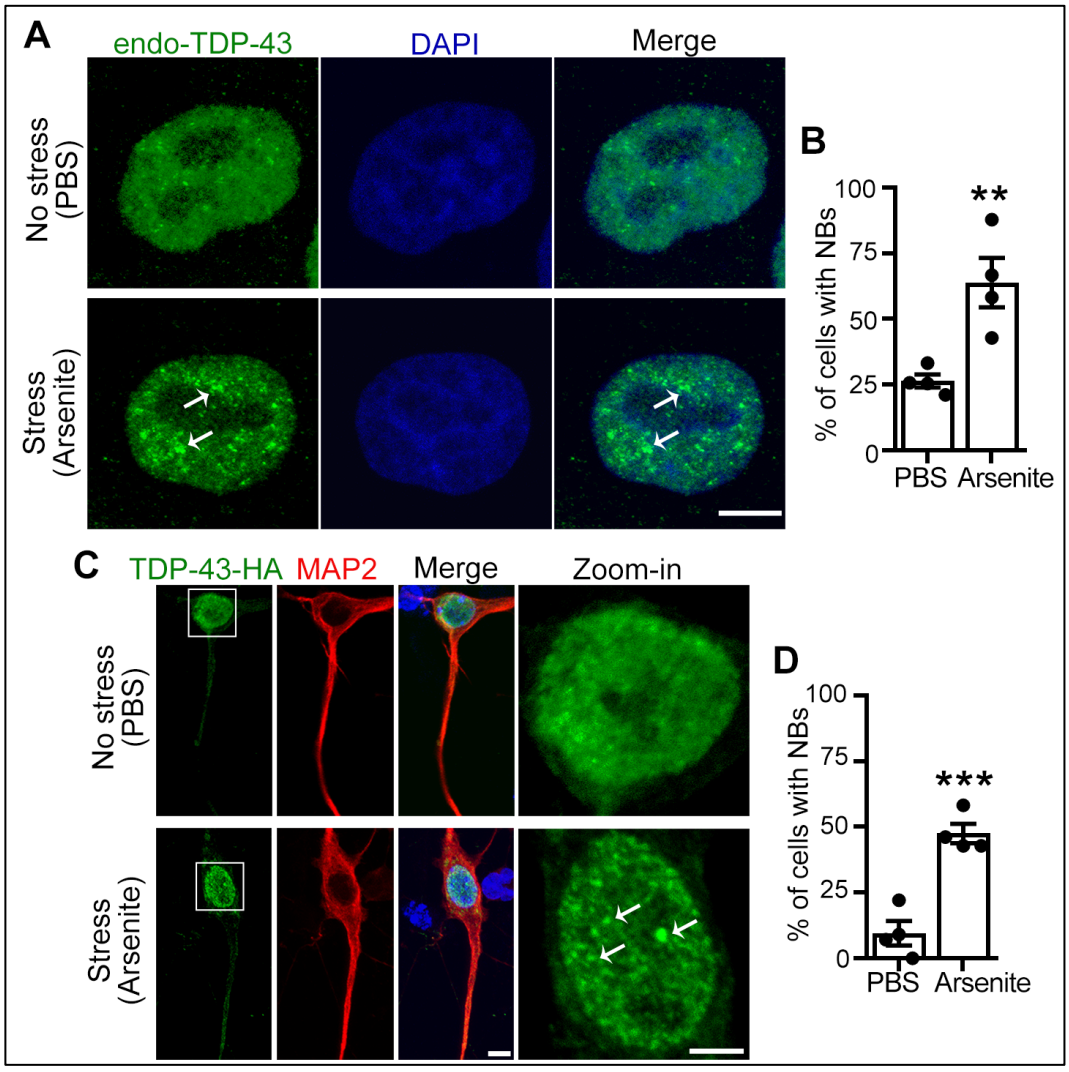

Figure S2. Stress-induced NBs are observed with endogenous TDP-43 and in primary neurons

(**A-B**) Representative images of endogenous TDP-43 (endo-TDP-43) forming NBs upon arsenite treatment (500 μM, 30 min). DAPI staining to show the nucleus and merged images are also shown. Percentage of cells showing distinct TDP-43 NBs in (A) is quantified in (B). Arrows indicate TDP-43 NBs. (**C-D**) Representative images (C) and quantification (D) of TDP-43-HA NBs in primary mouse cortical neurons induced by arsenite treatment. TDP-43-HA (green), microtubule associated protein 2 (MAP2) to mark neuronal perikarya and dendrites (red), and merged images with DAPI staining to label the nucleus (blue) are shown. Zoom-in images of the boxed areas are also shown. Mean ± SEM, n = 100 cells each group from pooled results of 3 independent repeats; $^{**}p < 0.01$, $^{***}p < 0.001$; Student's *t*-test. Scale bars: 5 μm in (A and C), and 2 μm in the zoom-ins.

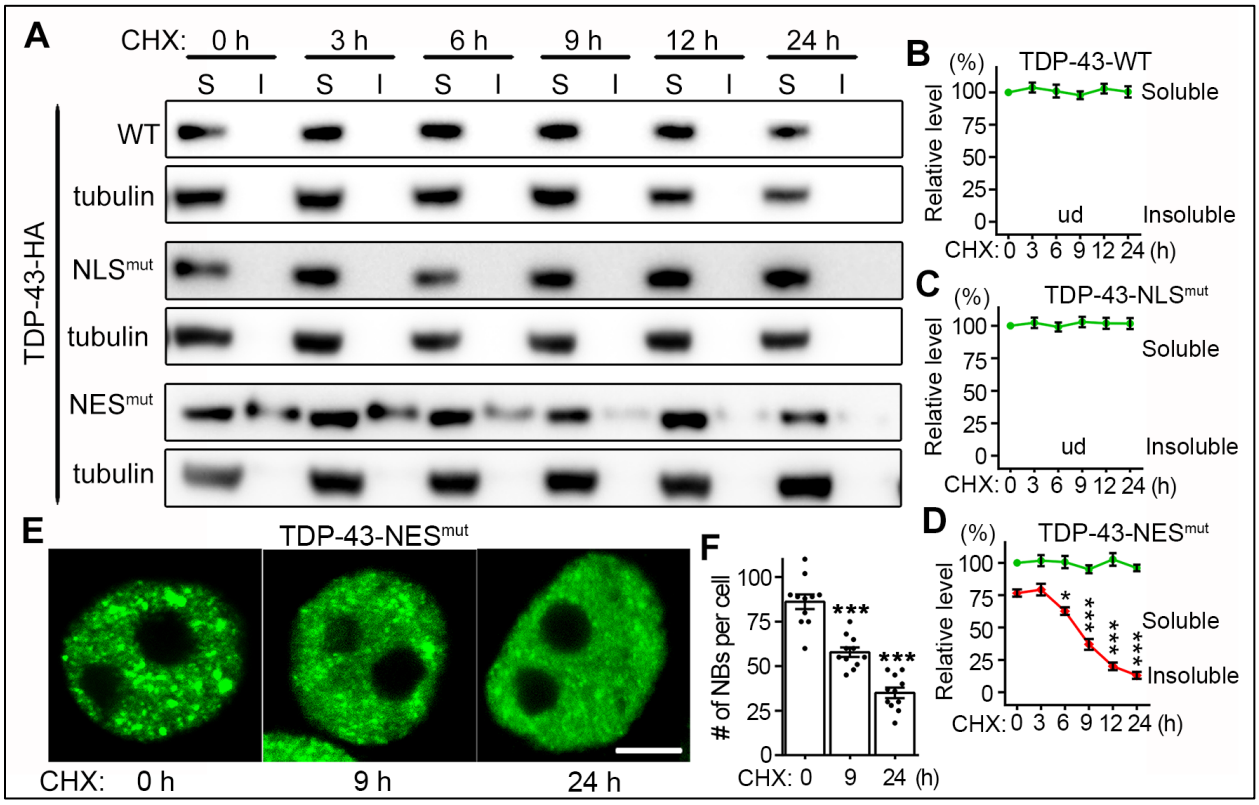

Figure S3. TDP-43-NES^{mut} NBs are dynamic and reversible

(**A-D**) Representative Western blot images (A) and quantifications (B-D) of the pulse-chase experiments of WT, NLS^{mut} and NES^{mut} TDP-43 protein in the soluble (S, supernatants in RIPA) and the insoluble (I, pellets resuspended in 9 M of urea) fractions at indicated time after Cycloheximide (CHX) treatment. All proteins are normalized to tubulin in the soluble fraction and the relative level at 0 h is set to 100%. Mean ± SEM, n = 3 independent repeats; compared to the level at 0 h; *P < 0.05, ***P < 0.001; ud, undetected; one-way ANOVA. (**E**) Representative images showing TDP-43-NES^{mut} NBs in 293T cells at indicated time after CHX treatment. (**F**) Quantification of the average number of TDP-43 NBs per cell in (E). Mean ± SEM, n = 10~11 cells per time point, from pooled results of 3 independent repeats; ***p < 0.001; one-way ANOVA. Scale bar: 5 μm.

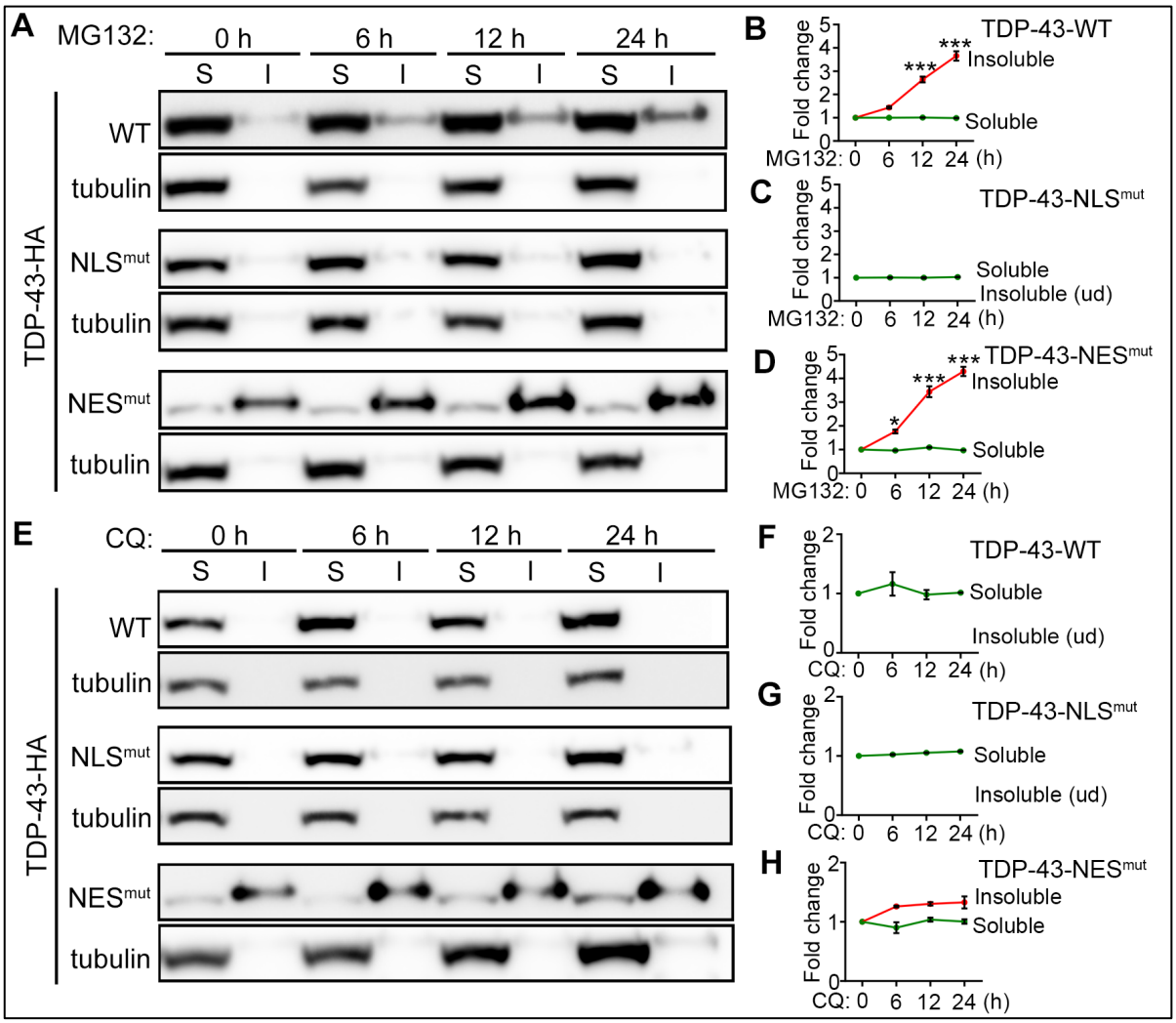

Figure S4. The turnover of insoluble TDP-43 is sensitive to proteasomal but not autophagic inhibition

(**A-D**) Representative images (A) and quantifications (B-D) of Western blotting analyses of WT, NLS^{mut} and NES^{mut} TDP-43 in the soluble (S) and insoluble (I) fractions at indicated time after treating the cells with MG132 to inhibit the proteasome-mediated protein degradation. (**E-H**) Representative images (E) and quantifications (F-H) Western blot analyses of WT, NLS^{mut} and NES^{mut} TDP-43 in the soluble (S) and insoluble (I) fractions at indicated time after treating the cells with chloroquine (CQ) to block the autophagic flux. S, supernatants in RIPA; I, precipitates in RIPA that are re-suspended in 9 M of urea. All proteins are normalized to tubulin in the soluble fraction and the relative level of each fraction at 0 h is set to 1. Mean ± SEM, n = 3 independent repeats; *P < 0.05, ***p < 0.001; ud, undetected; one-way ANOVA.

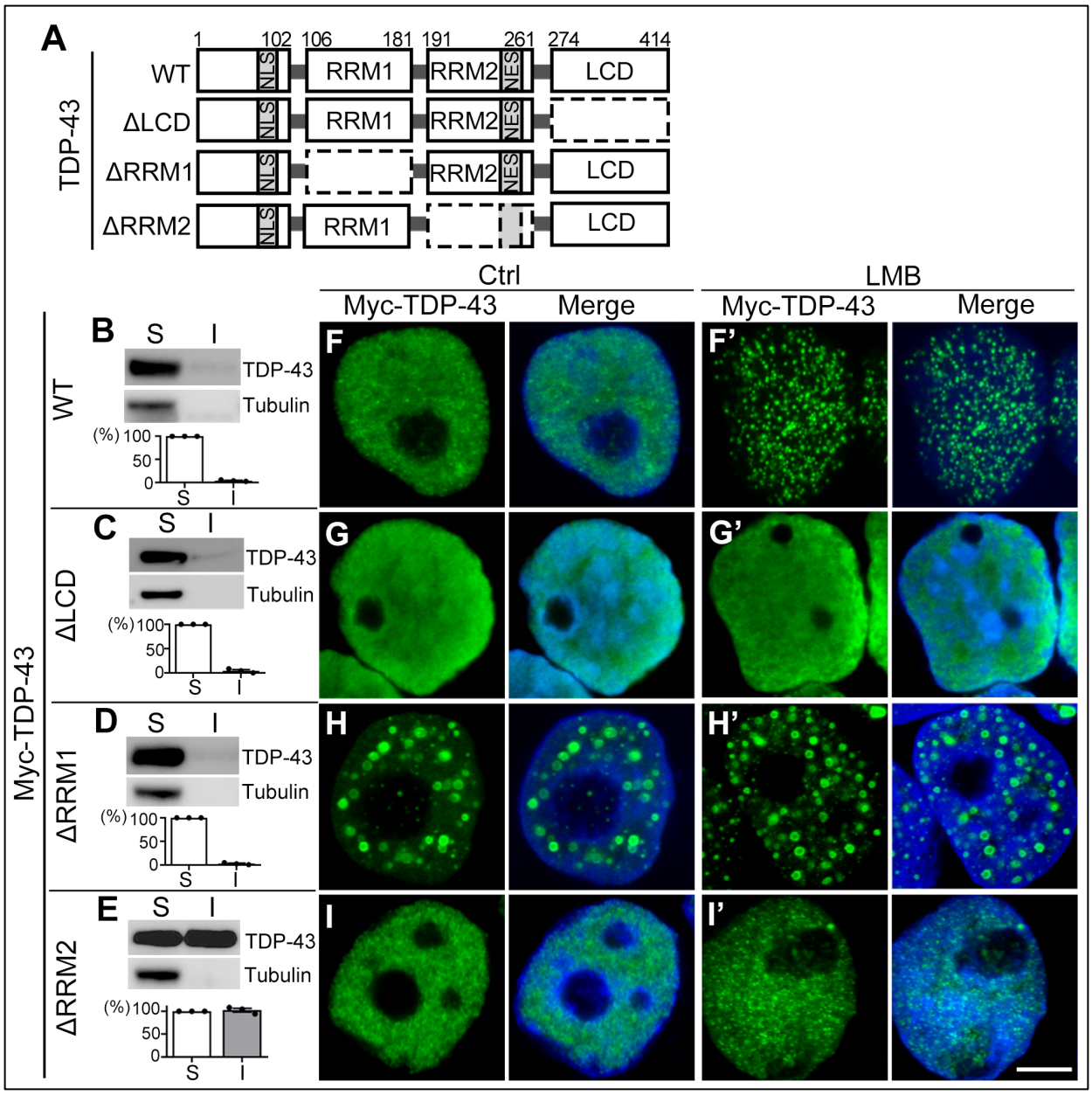

Figure S5. The impact of the LCD and RRM domains on the assembly of TDP-43 NBs

(**A**) A diagram showing the major functional domains and the truncated ΔLCD, ΔRRM1 and ΔRRM2 TDP-43. (**B-E**) Western blot analysis of TDP-43-WT (B), ΔLCD (C), ΔRRM1 (D) and ΔRRM2 (E) in the RIPA-soluble and RIPA-insoluble (resuspended in 9 M of urea) fractions. All TDP-43 proteins are normalized to tubulin in the soluble fraction and the relative level is quantified as percentage to the soluble fraction of each protein. Mean ± SEM, n = 3 independent repeats. (**F-I'**) Representative confocal images of TDP-43-WT, ΔLCD, ΔRRM1 and ΔRRM2 in 293T cells treated with the vehicle control ethanol (F-I) or LMB (F'-I'). Green, anti-Myc for Myc-TDP-43; blue, DAPI for DNA. Scale bar: 5 μm.

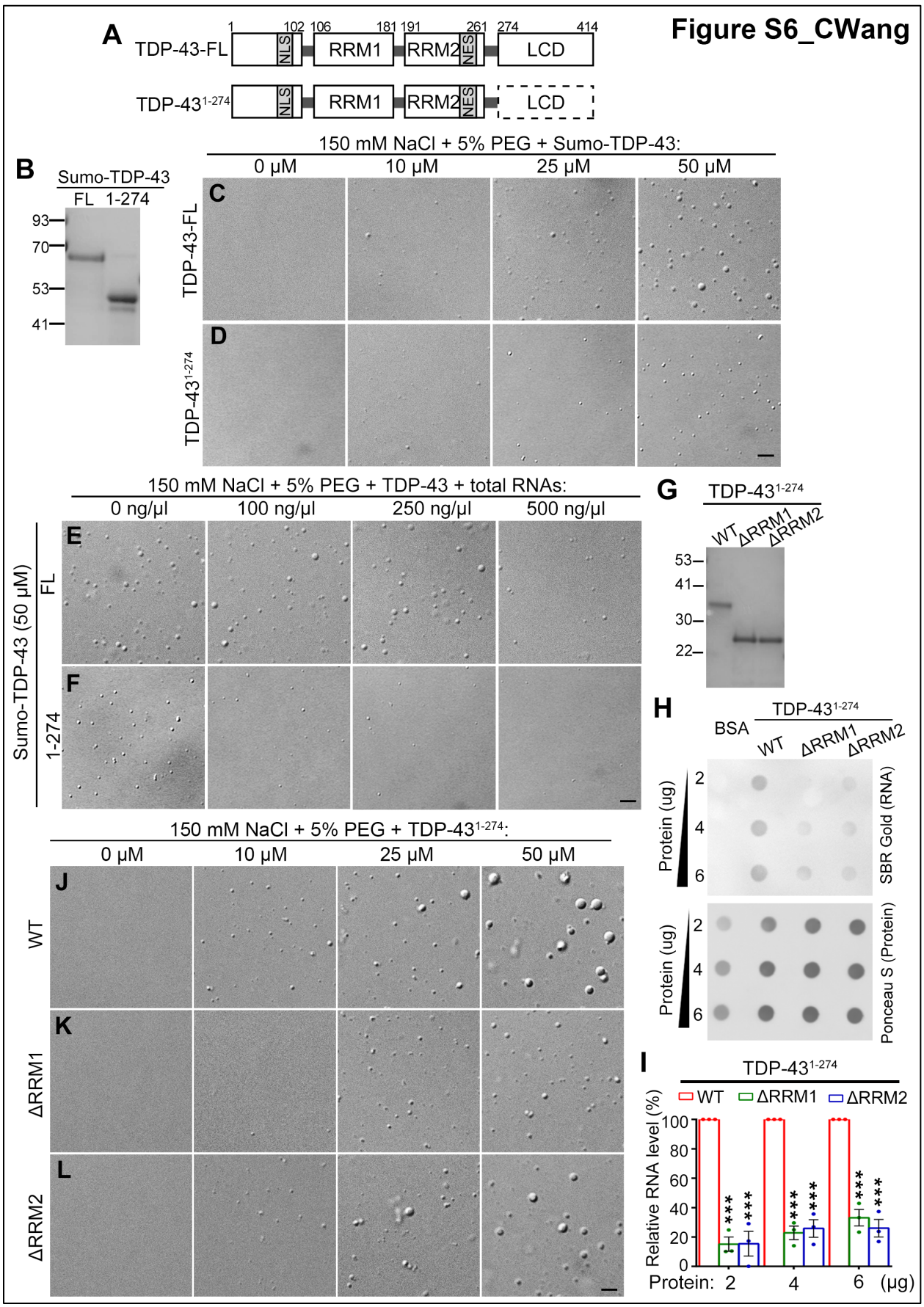

Figure S6. Total RNAs suppress TDP-43 LLPS *in vitro*

(**A**) A diagram showing the full-length (FL) and truncated TDP-43 protein without the LCD (TDP-$43^{1\text{-}274}$). (**B**) Coomassie blue staining confirming the purified FL and truncated sumo-TDP-43 proteins. (**C-D**) The *in vitro* LLPS of FL (C) and TDP-$43^{1\text{-}274}$ (D) is dose-dependent. (**E-F**) Suppression of the LLPS of the FL and the TDP-$43^{1\text{-}274}$ by total RNAs extracted from HeLa. (**G**) Coomassie blue staining confirming purified WT, ΔRRM1 and ΔRRM2 TDP-$43^{1\text{-}274}$ proteins used in the *in vitro* assays below and in Figure 6. (**H**) Representative images of the *in vitro* dot-blot assay confirming the reduced RNA binding affinity of the ΔRRM1 and ΔRRM2 TDP-$43^{1\text{-}273}$ compared to the WT. The bound RNA is visualized using the SYBR® Gold Nucleic Acid Gel Stain kit. Bovine serum albumin (BSA) is used as a negative binding control. (**I**) The RNA intensity is normalized to Ponceau S staining (protein loading control) and shown as the percentage to that of WT TDP-$43^{1\text{-}273}$ in (H). Mean ± SEM, n = 3; ***$p < 0.001$; Student's *t*-test. (**J-L**) WT (J), ΔRRM1 (K) and ΔRRM2 (L) TDP-$43^{1\text{-}273}$ proteins forms LDs *in vitro* by LLPS in a dose-dependent manner. The concentrations of NaCl, the crowding agent PEG, TDP-43 protein and total RNAs used in the above assays are as indicated. Scale bars: 2 μm.

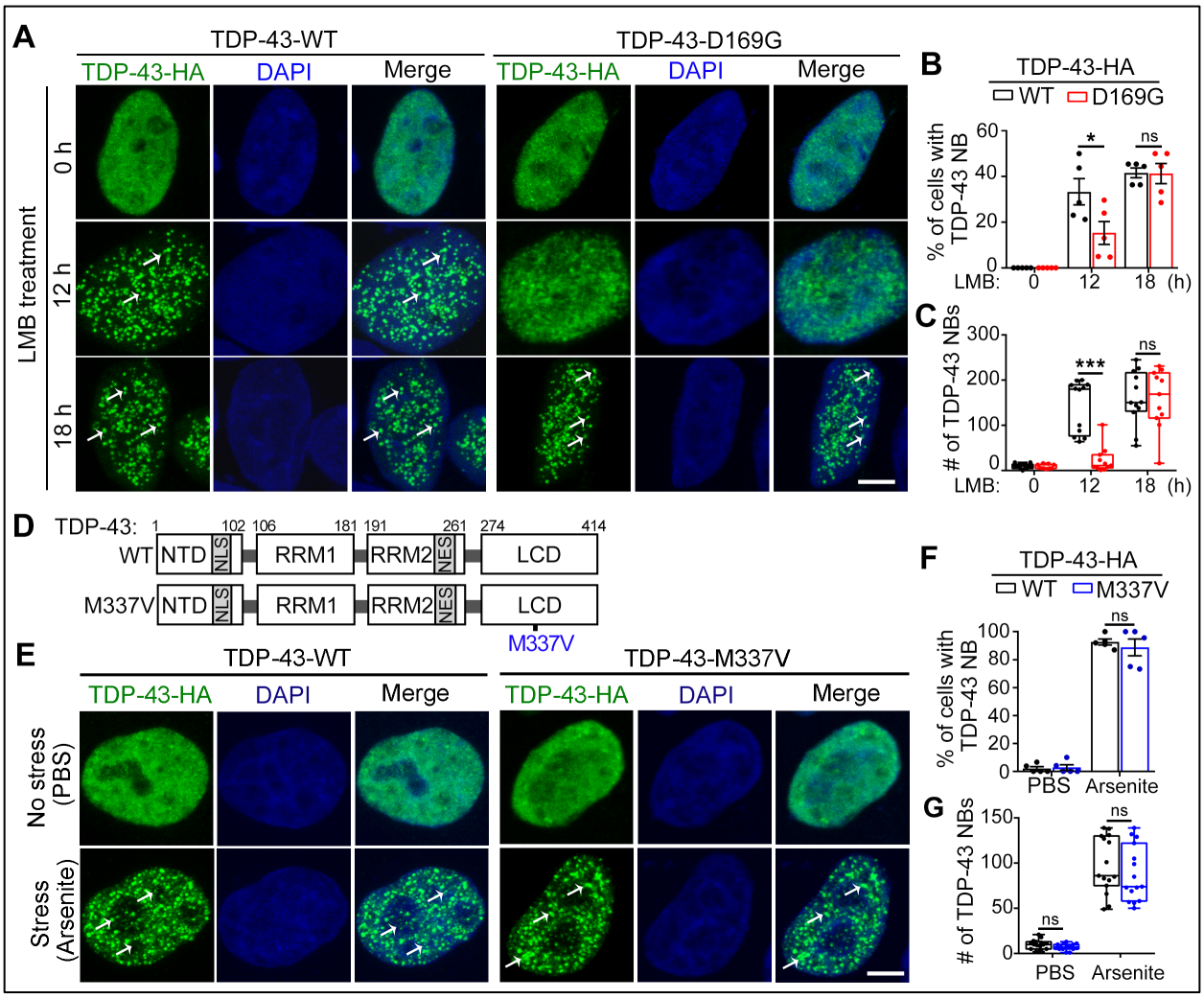

405

406 **Figure S7. The D169G mutant TDP-43 has a specific defect in NB formation**

407 (**A**) Representative confocal images of HeLa cells expressing with WT or D169G TDP-43 treated
408 with LMB for indicated times. (**B-C**) Quantifications of the percentage of cells showing TDP-43
409 NBs (B) and the average number of NBs per cell (C) at the end of the experiment in (A).
410 LMB-induced NB formation was delayed in D169G TDP-43. (**D**) A diagram showing WT TDP-43
411 and the M337V mutation in the LCD. (**E**) Representative confocal images of cells transfected
412 with WT or M337V TDP-43 in the absence (PBS) or presence of arsenite. Green, TDP-43-HA
413 (anti-HA); Blue, DAPI staining for DNA (blue); arrows, TDP-43 NBs. (**F-G**) The percentage of
414 cells with TDP-43 NBs (F) and the average count of TDP-43 NBs per cell (G) in (E) are quantified.
415 Mean ± SEM, n = ~100 cells in total for each group in (B, F) and 11~15 cells per group in (C, G),
416 pooled results from 3 independent repeats; *$p < 0.05$, ***$p < 0.001$; ns, not significant; Student's
417 *t*-test. Scale bars: 5 μm.

Supplementary movies

Movie S1. A representative time-lapse video of *live* HeLa cells showing the formation of GFP-TDP-43 NBs upon the arsenite treatment

Movie S2. A representative time-lapse video of GFP-TDP-43-GFP NBs in *live* HeLa cells before and after photobleaching